Role of convection in particle deposition at solid surfaces

Zbigniew Adamczyk*, Piotr Warszyński, Lilianna Szyk-Warszyńska,
Paweł Weroński *

Institute of Catalysis and Surface Chemistry, Polish Academy of Sciences, ul. Niezapominajek 1, 30-239 Cracow, Poland

Abstract

Recent theoretical and experimental data concerning colloid particle deposition from well-defined flows onto solid/liquid interfaces were reviewed. The macroscopic flow fields in the vicinity of the spherical and cylindrical collector (both isolated and forming a structured layer) were presented. Analogous solutions for the impinging-jet cells of (i) radial symmetry (radial impinging-jet cell RIJ) and (ii) plane symmetry (the slot impinging-jet cell SIJ) were also discussed. Similarities and differences between these flows are pointed out. The method of decomposing the macroscopic flows into local flows of simple geometry like shearing and stagnation flows was exposed. The microscopic flows are discussed in some detail, especially those connected with the motion of a spherical particle parallel and perpendicular to a solid wall. Using the local flow distributions the governing continuity equation is formulated, incorporating the convective transport in the bulk and the specific force dominated transport at the surface. Approximate analytical models aimed at decoupling these transfer steps are described, in particular the surface force boundary layer approximation (SFBLA). Limiting analytical solutions for the perfect sink boundary conditions were given. A procedure of extending the convective diffusion theory to non-linear adsorption regimes governed by the steric barrier due to adsorbed particles, was also presented. The role of the electro-hydrodynamic coupling leading to the hydrodynamic scattering effect in the blocking phenomena was discussed. The theoretical results are confronted with experimental data obtained in the well-defined systems, e.g. mostly in the RIJ and SIJ cells using monodisperse polystyrene latex colloids. A good agreement of theoretical and experimental data was found and most of the theoretical predictions were quantitatively confirmed, in particular the significance of the hydrodynamic scattering effect. © 2000 Elsevier Science B.V. All rights reserved.

Keywords: Convective effects in particle deposition; Colloid particle deposition; Deposition of particles of collectors; Hydrodynamic effects in colloid deposition

1. Introduction

Adsorption and deposition (irreversible adsorption) of colloid and bioparticles at solid–liquid interfaces is of great significance for many natural and practical processes such as water and waste water filtration, membrane filtration, papermaking, flotation, protein and cell separation, immobilisation of enzymes, biofouling of membranes and artificial organs, etc. A quantitative analysis of particle adsorption phenomena, viewed as the limiting form of heterocoagulation, can also fur-

_____
* Corresponding author.

nish interesting information on specific interactions under dynamic conditions which has implications for colloid science, biophysics and medicine, soil chemistry, etc. Furthermore, by measuring particle deposition in model systems, e.g. monodisperse colloid suspension, important clues can be gained concerning mechanisms and kinetics of molecular adsorption difficult for direct experimental studies. In this way various aspect of statistical–mechanical theories can be tested and links between irreversible (colloid) and reversible (molecular) systems can be established.

It should be pointed out; however, that colloid particle adsorption is proceeding via more complicated path than molecular adsorption being to a large extent influenced by hydrodynamic and external force fields (e.g. gravity, magnetic electrostatic). Although, the role of hydrodynamics is rather complex, the following two effects seem to be decisive [1,2]; (i) transport of particles over macroscopic distances (convection) toward interfaces where they become subject to specific force fields and (ii) microscopic scale coupling between local shearing flows and electrostatic repulsive interactions leading to enhanced surface blocking (referred often to as hydrodynamic scattering [3]). These effects are conveniently studied under well-defined conditions using the stagnation flow cells [4–10]. Usually the number of particles adsorbed in these cells is determined directly via optical microscopy [3–10] whereas for particle size below 0.1 μm indirect methods are applied such as ellipsometry [11] or reflectometry [12–15].

On the other hand, in practice, especially in various filtration procedures, the adsorber surface (collector) is of a spherical (packed bed columns) or cylindrical (fibers) shape.

Therefore, the aim of our work is to review recent experimental data obtained using these cells and to present ways of transferring this information to more complicated collector geometry occurring in practice.

The organisation of our paper is the following: in the first chapter we analyse the macroscopic flow fields in the vicinity of the spherical and cylindrical collector (both isolated and forming a structured layer). Analogous solutions for the impinging-jet cells of (i) radial symmetry (radial impinging-jet cell RIJ) and (ii) plane symmetry (the slot impinging-jet cell SIJ) are discussed next. Similarities and differences between these flows are pointed out. The method of decomposing the macroscopic flows into simple shear and stagnation flows in the vicinity of interfaces is also exposed. Then, the microscopic flows are discussed in some detail, especially the motion of a spherical particle parallel and perpendicular to a solid wall. Using the local flow distributions the governing continuity equation is formulated, incorporating the convective transport in the bulk and the specific force dominated transport at the surface. Approximate analytical models aimed at decoupling these transfer steps are described, in particular the powerful surface boundary layer approximation (SFBLA). A procedure of extending this model to non-linear adsorption regimes governed by the steric barrier due to adsorbed particles, is presented. The role of the hydrodynamic scattering effect in enhancing the blocking phenomena is discussed. The theoretical results are confronted with experimental data obtained in the well-defined systems, e.g. mostly in the RIJ and SIJ cells using monodisperse polystyrene latex colloids.

2. Macroscopic flow fields

Any motion of the Newtonian fluid can be described in terms of the Navier–Stokes equation

$$\rho\left(\frac{\partial v}{\partial t} + V\cdot\nabla V\right) = -\nabla p + \eta\nabla^2 V + F \tag{1}$$

where V is the fluid flow velocity, ρ is the fluid density, p is the pressure, η is the dynamic viscosity, F is the body volume force exerted on the fluid and t is the time. For the incompressible liquids the Navier–Stokes equation is complemented by the continuity equation

$$\nabla \cdot V = 0 \tag{2}$$

To solve Eqs. (1) and (2) for the fluid velocity V, the initial velocity field and boundary condition must be specified. The Navier–Stokes equation is a highly non-linear equation and complete analytical solutions exists for simple geometries

only. In most cases it is necessary to apply sophisticated numerical algorithms. In many processes the steady state is established very fast and it is sufficient to consider the steady fluid motion. Then, the time derivative $\partial V/\partial t$ can be neglected.

In general the presence of the dispersed phase changes the properties of the liquid. If the concentration of the dispersed colloidal particles is high the fluid usually exhibits viscoelastic behaviour [16]. For the moderate concentrated suspension it is sufficient to adjust the viscosity of the fluid for the presence of colloidal particles [17]. If the volume fraction of the particles is less than 5%, which corresponds to a particle concentration of the order of 10^{12} cm^{-3} in the case of typical colloids, the influence of particles on the flow around the macroscopic interfaces can be neglected.

The review of the macroscopic flow fields being the solution of the Navier–Stokes equation for the collectors of various geometries relevant for the practical applications of adsorption of col-

loidal particles was presented in the monographs by van de Ven [17], Elimelech et al. [18] and in the review articles by Adamczyk et al. [1–3].

Among numerous collector geometries we discuss here in some details the spherical and cylindrical collector, both isolated and forming a structured layer, and impinging-jet cells of radial and planar symmetry (see Fig. 1).

2.1. Sphere in uniform flow

In the case of a sphere immersed in the uniform flow one may conveniently solve the Navier–Stokes equation in the spherical coordinates (r, ϑ) by introducing the stream function Ψ. The components of the fluid flow velocity are then given by [19]

$$V_r = -\frac{1}{r^2 \sin \vartheta} \frac{\partial \Psi}{\partial \vartheta}$$

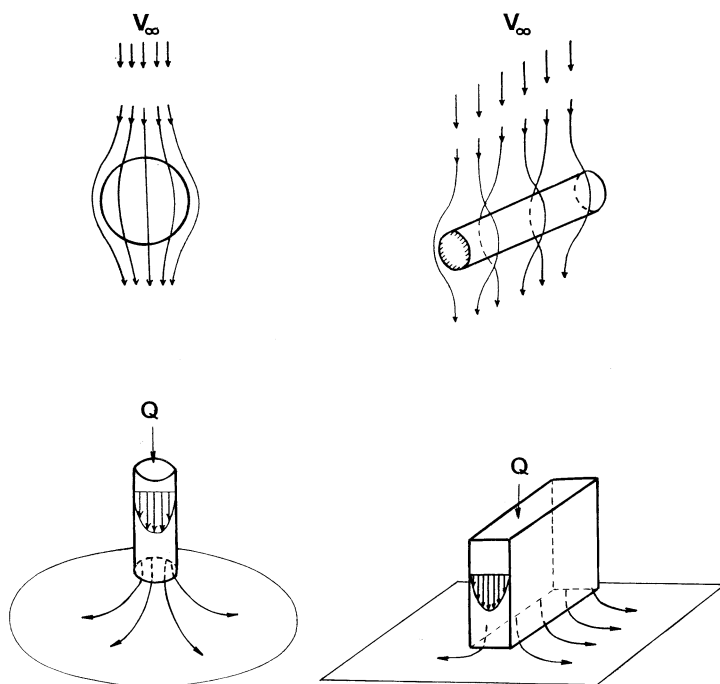$$V_\vartheta = \frac{1}{r \sin \vartheta} \frac{\partial \Psi}{\partial r} \tag{3}$$

Fig. 1. A schematic view of the laminar flow pattern in the vicinity of sphere in uniform flow, cylinder in uniform flow radial impinging-jet (RIJ) cell and the slot impinging-jet cell (SIJ). V_∞ is the velocity of the uniform flow and Q is the volume flow.

For low Reynolds number, $Re = 2V_\infty R/v \ll 1$ (where V_∞ is the uniform flow velocity cf. Fig. 1, R is the sphere radius and $v = \eta/\rho$ is the fluid kinematic viscosity) the stream function around a sphere can be expressed as:

$$\Psi = \frac{1}{2}V_\infty R^2 \sin^2 \vartheta \left[\frac{1}{2\bar{r}} - \frac{3}{2}\bar{r} + \bar{r}^2 \right] \tag{4}$$

where $\bar{r} = r/R$.

Using Eq. (3) one can derive the following expressions for the velocity components

$$V_r = -\frac{1}{2}V_\infty \left[2 - \frac{3}{\bar{r}} + \frac{1}{\bar{r}^3} \right] \cos \vartheta$$

$$V_\vartheta = -\frac{1}{4}V_\infty \left[\frac{3}{\bar{r}} + \frac{1}{\bar{r}^3} - 4 \right] \sin \vartheta \tag{5}$$

For small distances from the interface, when $\bar{h} = (r - R)/R \ll 1$, Eq. (5) simplifies to

$$V_r = -\frac{3}{2}V_\infty \bar{h}^2 \cos \vartheta$$

$$V = \frac{3}{2}V_\infty \bar{h} \sin \vartheta \tag{6}$$

It was shown in [1,17] that for $Re \ll 300$ one can still use Eq. (6) written in the form

$$V_r = -\frac{3}{2}A_f V_\infty \bar{h}^2 \cos \vartheta$$

$$V_\vartheta = \frac{3}{2}A_f V_\infty \bar{h} \sin \vartheta \tag{7}$$

where the dimensionless flow parameter A_f increases with the Reynolds number according to the expression [20]

$$A_f = \frac{3}{2}\left[1 + \frac{0.19Re}{1 + 0.25Re^{0.56}} \right]$$

If we consider the porous medium composed of identical spheres of radius R, the flow field around a single sphere is influenced by presence of other spheres. Various models that describe the flow field in the packed bed consisting of spheres are available. The 'sphere in cell' models [21–23] consider that each sphere in the porous plug is surrounded by the spherical cavity filled with fluid. The size of cavity is determined by the overall average porosity of the medium. The general solu-

tion of the Navier–Stokes equation for the stream function inside the cavity may be written as [18]:

$$\Psi = \frac{1}{2}V_\infty R^2 \sin^2 \left[K_1 \frac{R}{r} + K_2 \frac{r}{R} + K_3 \left(\frac{r}{R} \right)^2 \right.$$
$$\left. + K_4 \left(\frac{r}{R} \right)^4 \right] \tag{8}$$

where the coefficients K_{1-4} are to be determined from the boundary conditions at the surfaces of the cavity. On the inner surface of the cavity, i.e. at the sphere surface, the usual no-slip boundary conditions are used. The boundary conditions at the outer surface of the cavity depend on the model of the porous medium. Knowing the expression for the stream function the velocity component can be calculated applying Eq. (3). Using Happel's no stress boundary conditions at the outer surface of the cavity [22,24] and introducing the dimensionless $\bar{h}$ coordinate one can express the fluid velocity components close to the surface of the sphere in the form analogous to Eq. (7) with the flow parameter given by

$$A_f = \frac{2(1 - P^5)}{w} \tag{9}$$

where $P = R/b = (1 - \varepsilon_p)^{1/3}$ and $w = 2 - 3P + 3P^5 - 2P^6$, b being the radius of the cavity and ε_P is the average porosity of the medium. A similar expression can be obtained using the model of Kubawara [23] by assuming no vorticity boundary condition at the outer surface of the cavity.

The second class of models of the fluid flow through the packed bed of identical spheres is based on the swarm theory [25,26] to include the effects of the flow in the porous medium surrounding the cavity which is usually considered in terms of either Darcy's or Brinkman's law. The flows inside and outside the cavity must satisfy the continuity boundary conditions at its outer surface. The models based on the swarm theory describe better the fluid flow in the media of lower porosity than the sphere-in-cell models.

2.2. Cylinder in uniform flow

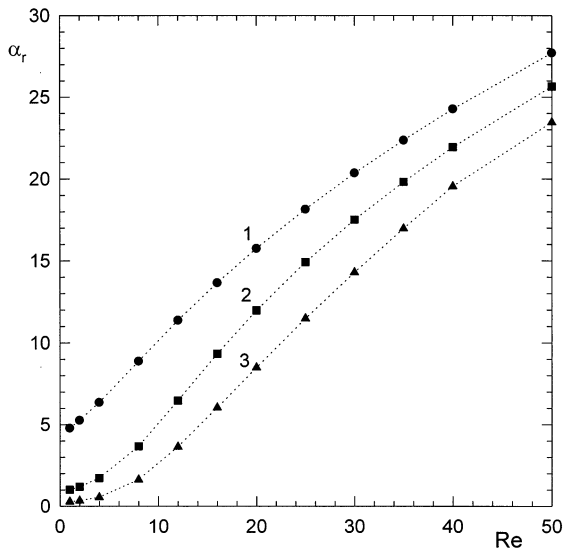The Navier–Stokes equation for the motion of fluid around the isolated stationary cylinder can

Fig. 2. The dependence of the flow parameter α_r on the Reynolds number calculated for various RIJ cell geometry. Spline curves, 1 for $h_c/r_c = 1$, 2 for $h_c/r_c = 2$ and 3 for $h_c/r_c = 3$ are fitted to the points obtained from the numerical solution of the Navier–Stokes equation.

be conveniently formulated in the cylindrical polar coordinates (ρ, ϑ). However, an exact solution for the low Re is not possible due to a divergence problem (Stokes' paradox). At small distances from the cylinder surface the components of the fluid flow velocity can be approximated by [27]:

$$V_\rho = -2A_f V_\infty \bar{h}^2 \cos \vartheta \qquad (10)$$

$$V_\vartheta = 4A_f V_\infty \bar{h} \sin \vartheta$$

where R is the cylinder radius and

$$A_f = 2(\beta - 0.48\beta^3), \ \beta = (2.022 - \ln Re)^{-1} \text{ for } Re$$
$$\leq 1 \text{ [26]}$$

$$A_f = 0.44 Re^{0.56} \text{ for } 1 < Re < 200 \text{ [26]}$$

It was also shown that for the porous plug formed by the network of identical cylinders one can derive a similar expression for the velocity components near the cylinder surface. For example for Happel model A_f is given by [22,27]

$$A_f = \left[1 + \left(\frac{\alpha^2 + 1}{\alpha^2 - 1} \right) \ln \alpha \right]^{-1} \qquad (11)$$

and for Kubawara model by [23,27]

$$A_f = \frac{\alpha - 1}{\ln \alpha + \dfrac{3}{2} - 2\alpha + \dfrac{1}{2}\alpha^2} \qquad (11a)$$

where $\alpha = 1 - \varepsilon_p$

The application of the swarm theory leads to more complicated formulas which can be found in [26].

2.3. Impinging-jet cells

The impinging-jet cells, shown in Fig. 1, appeared to be particularly useful for theoretical and experimental studies of colloidal particles adsorption. The first experimental cell having radial symmetry (RIJ) was constructed by Dąbroś and van de Ven [4,5]. Since then it has found numerous applications in the research on the adsorption of colloidal systems [3–15,28–32]. The fluid distribution in the cell can only be found in the general case by numerical solution of the governing Navier–Stokes equation [4]. However, for a small distance from the interface the fluid velocity components can be approximated by the expression [4]

$$V_r = \alpha_r(Re, h_c/r_c)V_\infty \bar{h} S_r(r) \qquad (12)$$

$$V_z = -\alpha_r(Re, h_c/r_c)V_\infty \bar{h}^2 C_r(r)$$

where h_c is the distance between the tip of the capillary and the interface, r is the radial distance from the symmetry axis, $\bar{h} = z/r_c$ is the dimensionless distance from the adsorbing interface, α_r is a flow parameter depending on the cell geometry and the flow intensity expressed by the Reynolds number $Re = Q/\pi r_c v$, where Q is the volume flow, r_c is the capillary radius and $V_\infty = Q/\pi r_c^2$ is the mean linear velocity. The dependence of α_r on Re for various h_c/r_c ratios is shown in Fig. 2. The functions $C_r(r)$ and $S_r(r)$ describing the radial distribution of the flow depend only on the radial coordinate. For $r/r_c < 0.25$, $C_r \approx 1$ and $S_r \approx r_c$.

Recently Adamczyk et al. [8,10] developed the new experimental cell shown schematically in Fig. 1 in which the suspension jet has plane-parallel geometry. The area accessible for the observation in this type of cell, usually called the 'slot-impinging jet' (SIJ), exceeds by order of magnitude that for the impinging-jet cells with cylindrical geome-
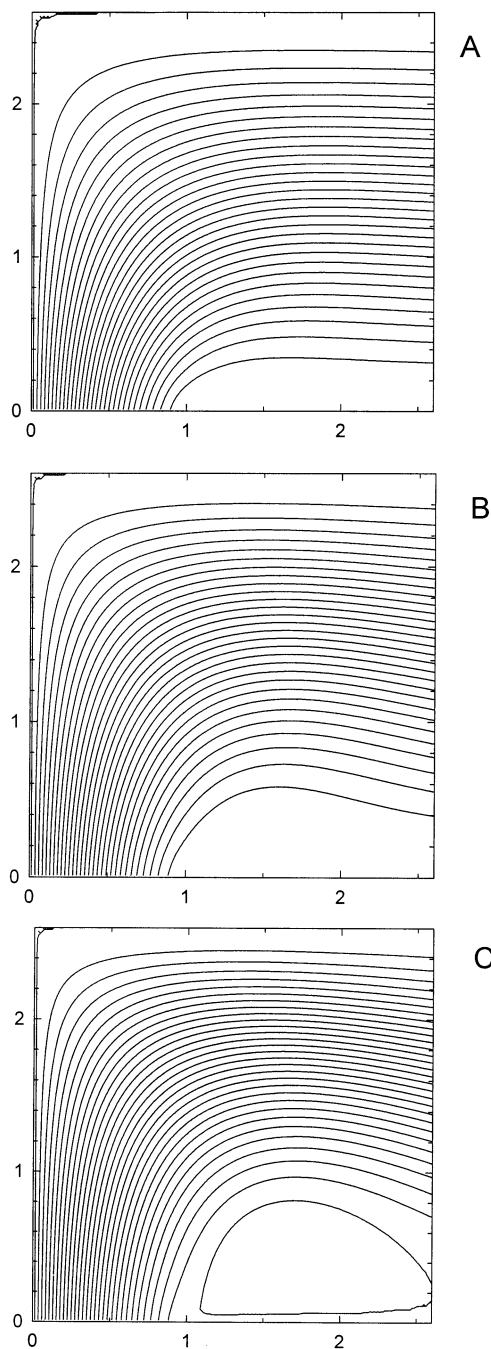
Fig. 3. Fluid streamlines in the SIJ cell ($h_c/d = 2.6$) determined from numerical solutions for A: $Re = 2$, B: $Re = 8$ and C: $Re = 16$. Due to symmetry, only the right-hand side of the cell is shown.

try. The fluid streamlines in the slot-impinging-jet cell obtained from the numerical solution of the Navier–Stokes equation are illustrated in Fig. 3. As it can be observed they exhibit a pattern typical for hyperbolic (stagnation) flows. A characteristic feature of the flow is that only a very small part of suspension jet entering the cell almost at the symmetry line has a chance to approach the interface close enough for particle adsorption to take place. For higher Reynolds number of the flow ($Re = V_\infty d/v$) a vortex is formed in the region adjacent to the inlet channel wall. A similar flow pattern is observed in the impinging-jet cell with cylindrical symmetry [4].

The flow field in the cell, near the interface can be described by [10]

$$V_x = 2\alpha_s(Re, h_c/d)V_\infty \bar{h}S_s(x) \qquad (13)$$

$$V_z = -\alpha_s(Re, h_c/d)V_\infty \bar{h}^2 C_s(x)$$

where x is the distance from the symmetry plane, α_s is the flow parameter which, is a function of the cell geometry and the Reynolds number of the flow, $V_\infty = Q/2dl$ where l is the depth of the channel assumed much larger than its width $2d$. The dependence of the flow parameter α_s on the Reynolds number and the ratio of the distance between the channel outlet and the adsorption surface to the channel half width (h_c/d) is shown in Fig. 4. The functions $S_s(x)$ and $C_s(x)$ describe the lateral distribution of the flow. Their dependence on the distance x from the symmetry line is shown in Fig. 5. It can be seen that for $x/d < 0.5$, $S_s(x) \approx x/d$ while for $x/d < 0.3$, $C_s(x) \approx 1$. It also can be noticed that the lateral dependence of the fluid flow velocity components in the slot-imping-ing-jet is very similar to the velocity components at the isolated cylinder (cf. Eq. (10)) if one defines $\vartheta = \pi x/2d$.

2.4. Decomposition of macroscopic flows

The above discussed fluid flow field in the vicinity of a macroscopic surface can be decomposed by using the local Cartesian coordinates (x_l, y_l, z_l) into the stagnation point flow V_{st} and a simple shear flow V_{sh} defined as:

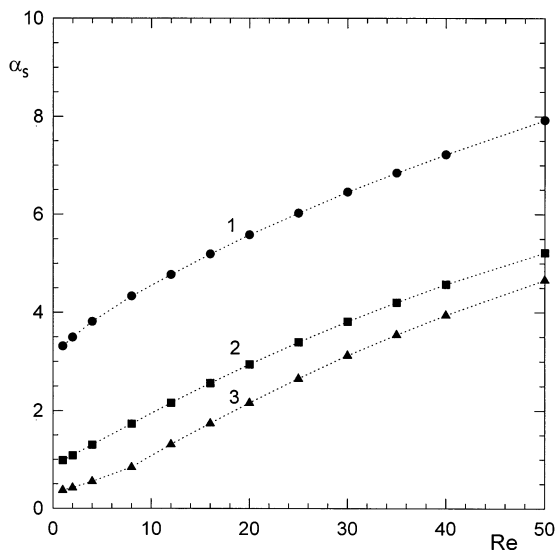$$V_{st} = G_{st}(2x_l z_l i_x - z_l^2 i_z)$$

Fig. 4. The dependence of the flow parameter α_s for SIJ cell on the Reynolds number calculated for various cell geometry. Spline curves 1 for $h_c/d = 1$, 2 for $h_c/d = 2$ and 3 for $h_c/d = 3$ are fitted to the points obtained from the numerical solution of the Navier–Stokes equation.

$$V_{sh} = G_{sh}z\boldsymbol{i}_x \qquad (14)$$

where G_{st} and G_{sh} are the stagnation point and simple shear flow strengths, respectively, $\boldsymbol{i}_x$ and $\boldsymbol{i}_z$ are the unit vectors in local Cartesian coordinates.

The fluid velocity components, the stagnation point and simple shear flow strength for all types of flows discussed in this review are collected in Table 1. Also values of the Peclet number, being a measure of the relative magnitude of convection and diffusion in the transport of suspension of colloidal particles to the surface, are presented. For a given type of flow the Peclet number is defined as: $Pe = V_{ch}a/D_\infty$ where V_{ch} is the characteristic fluid flow velocity close to the adsorption surface, a is the particle radius and D_∞ is particle diffusion coefficient in the unbound fluid.

3. Microscopic flow fields

A particle moving in the suspension produces a flow in the surrounding medium and surrounding walls. This flow exerts the viscous drag on the particle and its neighbours which can be consid-

ered as the long range hydrodynamic interaction. The problem of determining the fluid flow in a colloidal suspension is greatly simplified by the fact that the size of particles is of the order of micrometer or less. The resulting Reynolds number for this microscopic flow, $Re = aU_p/v$, where U_p is the typical velocity of particle motion becomes therefore very small, seldom exceeding 10^{-2}. Therefore, the Navier–Stokes equation can
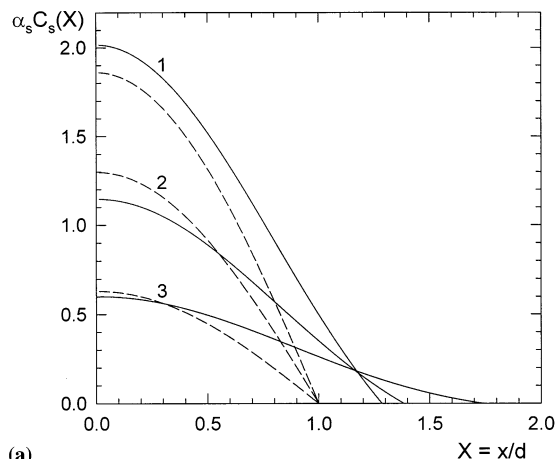
(a)
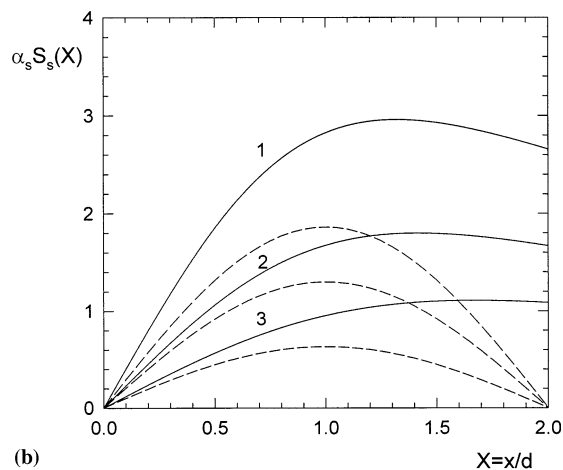
(b)

Fig. 5. (a) Dependence of $\alpha_s C_s (X)$ at $\bar{h} \to 0$ on the tangential coordinate X determined numerically for (1) $Re = 16$, (2) $Re = 8$ (3) $Re = 2$ (solid lines). The broken lines show the analytical solutions for a cylinder in a uniform flow, i.e. $\alpha_s C_s(X) = A_f \cos (\pi X/2)$, where $A_f = 0.44Re^{0.56}$. (b) Dependence of the $\alpha_s S_s(X)$ on X for (1) $Re = 16$, (2) $Re = 8$ and (3) $Re = 2$. The broken lines show the analytical solution for a cylinder in a uniform flow.

Table 1
Undisturbed flow fields near collectors

Collector	Velocity components	G_{st}	G_{sh}	Pe
Sphere in uniform flow	$V_r = -\dfrac{3}{2} A_f V_\infty \bar{h}^2 \cos \vartheta$ $V_\vartheta = -\dfrac{3}{2} A_f V_\infty \bar{h} \sin \vartheta$	$\dfrac{3 V_\infty A_f \cos \vartheta}{2 R^2}$	$\dfrac{3 V_\infty A_f \sin \vartheta}{2R}$	$\dfrac{3 A_f V_\infty a}{R^2 D_\infty}$
Cylinder in uniform flow	$V_\rho = -2 A_f V_\infty \bar{h}^2 \cos \vartheta$ $V_\vartheta = 4 A_f V_\infty \bar{h} \sin \vartheta$	$\dfrac{2 V_\infty A_f \cos \vartheta}{R^2}$	$\dfrac{4 V_\infty A_f \sin \vartheta}{R}$	$\dfrac{4 A_f V_\infty a^3}{R^2 D_\infty}$
Radial impinging jet 'RIJ' ($r/r_c < 0.25$)	$V_r = \alpha_r \dfrac{V_\infty}{r_c} \bar{h} r$ $V_z = -\alpha_r V_\infty \bar{h}^2$	$\alpha_r \dfrac{V_\infty}{r_c^2} r$	$\alpha_r \dfrac{V_\infty}{r_c^2} r$	$\dfrac{2 \alpha_r V_\infty a^3}{R^2 D_\infty}$
Slot impinging jet 'SIJ' ($x/d < 030$)	$V_x = 2\alpha_s \dfrac{V_\infty}{d} \bar{h} x$ $V_z = -\alpha_s V_\infty \bar{h}^2$	$\alpha_s \dfrac{V_\infty}{d^2}$	$2\alpha_s \dfrac{V_\infty}{d^2} x$	$\dfrac{2 \alpha_s V_\infty a^3}{d^2 D_\infty}$

be linearized and the resulting creeping flow (Stokes) equation for the uncharged particles has a form:

$$\eta \nabla^2 V = \nabla p \qquad (15)$$

The Stokes equation and the continuity equation, together with the appropriate boundary conditions on the particle surfaces and macroscopic interfaces form a complete boundary value problem. On the surface of the rigid particle or interface the no-slip boundary conditions are usually assumed while at a liquid/liquid interface the condition of equal stress at both sides of the interface is used.

Because of its relevance to practical applications, the hydrodynamic problem of the uncharged spherical particle moving close to the solid surface has been a subject of numerous works. Maude [33] and Bart [34] considered the problem of a sphere approaching a rigid plane interface, O'Neill solved the problem of a spherical particle sliding (moving without rotation) along the rigid plane [35,36] and attached at the surface in the simple shear flow [37], Dean and O'Neill gave the solution for the problem of the particle rotating at the rigid wall [38], while Goren and O'Neill solved the general hydrodynamic problem of the particle moving at the rigid wall in

a flow which velocity is of the second degree in the local coordinates [39]. The stagnation point flow, and the simple shear flow are the special cases of this general flow field. In all these papers the bispherical polar coordinates were applied and the fluid velocity fields were obtained analytically in terms of orthogonal functions expansions. These expansions are, however, slow converging if the distance between a particle and a rigid wall approaches zero. Therefore, Goldman, Cox and Brenner studied the problem of the spherical particle moving at the rigid wall in the lubrication approximation valid for the distances less then 20% of particle radius [40–42].

3.1. Sphere in the vicinity of planar wall in quiescent fluid

It was shown in [33,34] that the velocity of spherical particle moving in a quiescent fluid perpendicularly to the rigid wall is given by

$$U_\perp = F_1(H) \left(\frac{F_\perp}{6\pi\eta\, a} \right) = \frac{1}{\lambda_\perp(H)} \left(\frac{F_\perp}{R_{st}} \right) \qquad (16)$$

where $F_1(H)$ and $\lambda_\perp(H)$ are the correction function for the mobility and the Stokes resistance coefficient respectively, H is the width of the particle–wall gap normalized by particle radius,

$R_{st} = 6\pi\eta a$ is the Stokes resistant coefficient and $F_\perp$ is the component of the force causing particle motion directed perpendicularly to the wall and equal to the viscous drag force. The correction functions can be calculated analytically from the series [33,34]:

$$\lambda_\perp(H) = \frac{1}{F_1(H)}$$
$$= \frac{4}{3}\sinh(\alpha) \sum_{n=1}^{\infty} \frac{n(n+1)}{(2n-1)(2n+3)}\left[\frac{Y_n}{T_n} - 1\right] \quad (17)$$

where $\alpha = \cosh^{-1}(H)$ and

$$Y_n = 2\sinh(2n+1)\alpha + (2n+1)\sinh 2\alpha$$

$$T_n = 4\sinh^2(n+1/2)\alpha - (2n+1)^2\sinh^2\alpha$$

Since the exact form of Eq. (17) involving the sum of the infinite series is hard to implement, it is often useful to find effective interpolation function. Accordingly, it was found in [43] that the expression

$$F_1(H) = \frac{19H^2 + 4H}{19H^2 + 26H + 4} \quad (18)$$

provides a good approximation to the exact formula for the entire range of the gap width. The correction function $F_1(H)$ calculated using exact formula (Eq. (17)) and its approximation according to Eq. (18) are compared in Fig. 6.

The velocity of a spherical particle moving in the stagnant fluid parallel to the rigid wall can be obtained from:

$$U_{ll} = F_4(H)\left(\frac{F_{ll}}{6\pi\eta a}\right) = \frac{1}{\lambda_{ll}(H)}\left(\frac{F_{ll}}{R_{st}}\right) \quad (19)$$

where $F_4(H)$ and $\lambda_{ll}(H)$ are the correction function for the mobility and the Stokes resistance coefficient respectively and F_{ll} is the component of the force causing particle motion directed perpendicularly to the wall. The correction function $F_4(H)$ calculated by Goren and O'Neill [39] from the solution of the creeping flow equation in the bispherical polar coordinates is illustrated in Fig. 6 together with the interpolating function [43]:

$$F_4(H) = \frac{1}{1.062 - 0.516\ln(H)}; \text{ valid for } H < 0.11$$
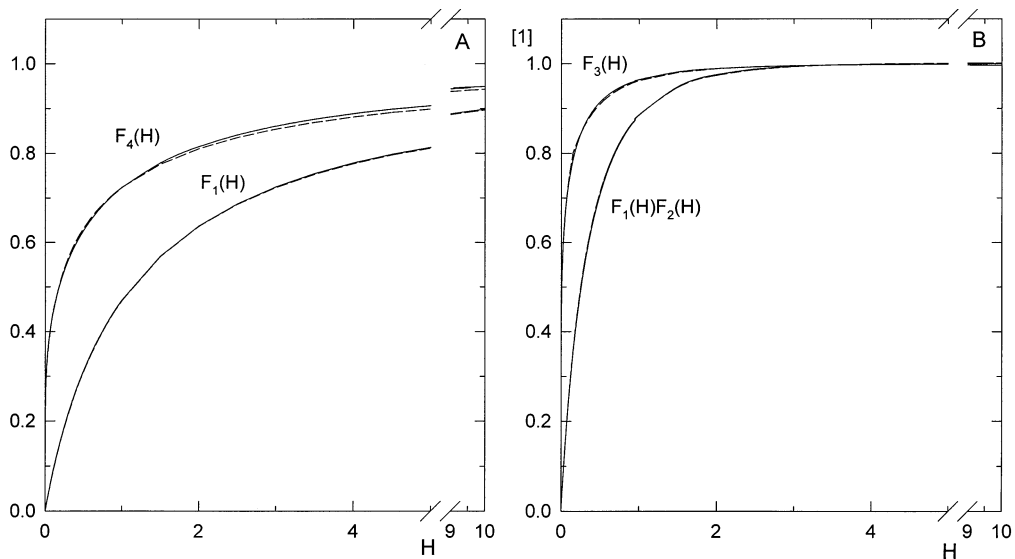

Fig. 6. The hydrodynamic correction functions for the spherical particle in the vicinity of the solid wall. Part A: the correction for a mobility of a freely moving particle perpendicular, $F_1(H)$, and parallel, $F_4(H)$, to the wall. Part B: the correction for the particle velocity moving towards the wall in the stagnation point flow $F_1(H)F_2(H)$ and along the wall in the simple shear flow $F_3(H)$. Solid lines show the results of exact solution of the creeping flow equation in the bispherical coordinates, dashed curves; the respective interpolation formulae (see text).

$$F_4(H) = \left(\frac{H}{2.639 + H}\right)^{1/4}; \text{ valid for } H \geq 0.11$$

$$(20)$$

The theoretical expressions describing the mobility of the particle close to a solid wall were verified experimentally by Adamczyk et al. [44] and Małysa and van de Ven [45] using multiple frame photography technique.

The universal correction functions $F_1 - F_4$ discussed in this section are used for constructing the mobility matrix needed for the bulk transport equation as discussed later on.

3.2. Sphere at a planar wall in presence of external flow

Since colloidal particle adsorption usually occurs in the presence of macroscopic flow it is important to describe also the influence of the hydrodynamic interactions on trajectory of particle moving in the external flow. When a particle is subjected to a flow in an unbounded fluid it follows the streamlines and the particle velocity is equal to the local fluid velocity. Due to the presence of the rigid interface the particle lags the fluid flow, i.e. the particle velocity differs from the local fluid velocity at the same point. As it was mentioned before, the fluid flow can be decomposed in the local Cartesian coordinates into the stagnation flow and simple shear flow, therefore, it is enough to discuss motion of particles in these flow fields.

In the stagnation flow if $V_\perp$ is the component of the fluid velocity perpendicular to the rigid wall, then the corresponding component of the particle velocity $U_\perp$ can be expressed as:

$$U_\perp = F_1(H)F_2(H)V_\perp \tag{21}$$

The correction function $F_2(H)$ was obtained from the analytical solution of the creeping flow equation by Goren and O'Neill [39]. The dependence of the product $F_1(H)F_2(H)$ on the particle–wall separation is shown in Fig. 6. The $F_2(H)$ function can be well approximated by [43]:

$$F_2(H) = 1 + \frac{1.79}{(0.828 + H)^{1.167}} \tag{22}$$

It can be seen that the interactions with the wall starts to influence the particle motion at distances $H < 2$ and for example at $H \simeq 0.25$ the particle velocity is 2 times lower than the local fluid velocity.

In the case of a particle moving in the simple shear flow particle velocity is a function of the shear rate G_{sh} and the distance to the wall H, i.e.

$$U_{ll} = F_3(H)G_{sh}a(1 + H) \tag{23}$$

where the dependence of the correction function $F_3(H)$ on the particle–wall separation determined by Goren and O'Neill [39] is illustrated in Fig. 6. It can be well approximated by the interpolation function [43]:

$$F_3(H) = \frac{1}{0.754 - 0.256 \ln(H)}; \text{ valid for } H$$

$$< 0.137$$

$$F_3(H) = 1 - \frac{0.304}{(1 + H)^3}; \text{ valid for } H \geq 0.137$$

$$(24)$$

The relationship between particle distance from the wall and its velocity in the simple shear flow (Eq. (23)) can be used for the experimental determination of the position of the particle relatively to the interface. Having measured particle velocity in the simple shear flow of the controlled intensity with the optical microscope, one can invert Eq. (23) and obtain particle–wall separation. Several authors have used this technique to study motion of colloidal particles at interfaces under the influence of the electric, electrokinetic, van der Waals, gravitational and steric forces [46–49].

3.3. Sphere/sphere attached at an interface

At the initial stage of the deposition process, when the surface coverage is low, the adsorption rate is determined by a particle–interface interactions only. When the coverage of the interface increases one has to take into account also the interactions of moving particles with the attached ones as well as the influence of the deposited particles on the flow field in the vicinity of the interface. On the other hand, the flowing particles can exert the influence on the adsorbed ones
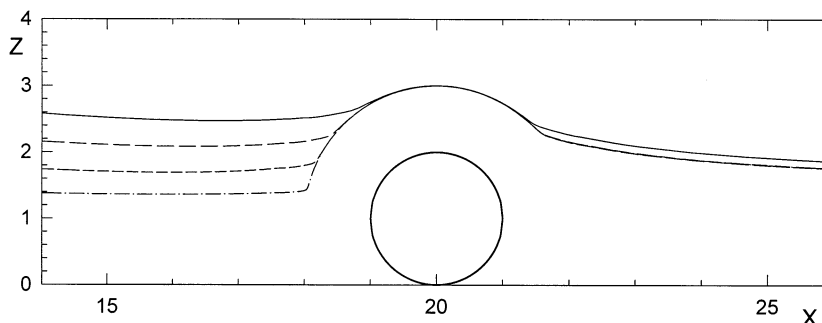
Fig. 7. The family of trajectories of a particle moving in the stagnation line flow around a particle attached to the wall obtained from the solution of creeping flow equation. The initial distance from the wall $Z_i = z_i/a$ ranged from 2.6 (the upper trajectory) to 1.4 (the lowest trajectory). The immobile particle centre was located at the distance $x_d/a = 20$ from the stagnation line.

leading to their desorption. Therefore, the proper description of the hydrodynamic interaction of moving colloidal particle with ones already deposited at the interface is of importance for the quantitative analysis of the adsorption process.

Due to the complicated geometry the solution of the creeping flow equation for the problem of many particles at interface is prohibitively complex and has been obtained only for the case of two particles by applying elaborate numerical techniques. In general the solution of the creeping flow (Stokes) equation can be expressed in the integral form [50]:

$$V(x) = V_0(x) + \sum_{l=1}^{2} S_l \, \underline{G}(x, y) \cdot f(y_l) \, \mathrm{d}S_l \tag{25}$$

where $V_0(x)$ denotes the fluid flow field at a given point in the absence of the particles fulfilling the no-slip boundary condition ($V_0 = 0$) at the interface, y is a vector pointing at the surface element $\mathrm{d}S_l$, $G(x, y)$ is the Oseen tensor accounting for the presence of the rigid wall [50], $f(y_l)$ is the force density at a point y_1 at the l ($l = 1, 2$) particle surface and S_l is the surface of particle l.

The total force F_l and torque T_l exerted by particle l on the fluid are given by the equations:

$$F_l = \int_{S_l} f(y_l) \, \mathrm{d}S_l \tag{26}$$

and

$$T_l = \int_{S_l} (y - R_l) \times f(y_l) \, \mathrm{d}S_l \tag{27}$$

where R_l specifies the position of the center of particle l.

In order to obtain a complete system of equations, one has to take into account the boundary conditions at the particle surface:

$$V(y_l) = U_l + \Omega_l \times (y_l - R_l) \tag{28}$$

where U_l and Ω_l are the translational and rotational velocities of the particle l, respectively. For the particle attached at the interface both velocities are equal to zero.

Eqs. (25)–(28) form a complete system, provided that the external force and torque or the velocities of the particles as well as the external flow field $V_0(x)$ are specified.

Dąbroś and van de Ven [51–53] developed two convenient methods of the numerical solution of the system of equations (Eqs. (25)–(28)) for the problem of two spherical particles at a rigid interface. In the first, the boundary element method (BEM), the surface of each particle is divided into a finite number of triangular elements. The surface integrals can be replaced by the sums of the integrals over the elements [52]. In the second method the particle surfaces are divided into a set of subunits and the surface integration in Eqs. (25), (26) and (28) can be replaced by summation over these subunits. A more detailed discussion of the subunit method with the application to the problem of the collision of two colloidal particles at the rigid interface can be found in [51,53].

The example of the hydrodynamic interactions between two spherical particles at the interface is

demonstrated in Fig. 7. This figure presents the trajectories of a spherical particles moving in the stagnation point flow and colliding with one firmly attached to the rigid planar interface at the distance of 20 particle radii from the stagnation point. The hydrodynamic interactions are taken into account using the multisubunit method while the hard core interaction between moving and stationary particle were considered in terms of Born-like interaction, proportional to h^{-9} where h is the particle–particle distance. It can be seen that during its motion along the interface the moving particle is repelled by the sitting one due to the hydrodynamic interactions. When the initial particle–wall gap width is greater then the particle diameter ($Z_i > 2$) the moving particle after the collision returns to the trajectory which would occur if the attached particle were not present. When the mobile particle is initially closer to the wall its trajectory, after the collision, significantly deviates from one in the absence of attached particle and is significantly pushed out of the interface.
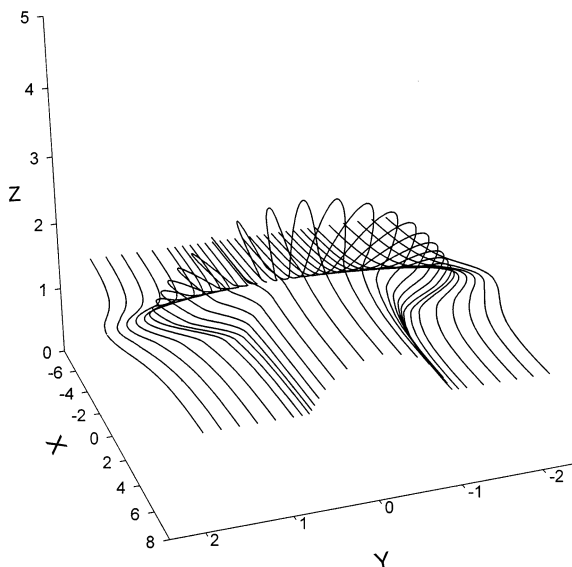

Fig. 8. The collision pattern formed by the trajectories of particles moving in the simple shear flow at the rigid wall and colliding with the particle firmly attached to it. The starting distance to the wall $Z_i = 1.6$ and the lateral position ranges from $Y_i = -2$ to $Y_i = 2$.

In Fig. 8 the family of particle trajectories is presented, calculated for the simple shear flow with the initial distance from the interface is $Z_i = z_i/a = 1.6$ and the lateral coordinate $Y_i = y_i/a$ of the starting position ranges from -2 to 2 and $X_i = x_i/a = -8$. It can be seen that the semicircular scattering pattern is formed by the final positions ($Y_f = 8$) of moving particles. The radius of this pattern is strongly dependent on the particle–particle interaction [43,53]. Thus, similarly as collisions of elementary particles, collisions of colloidal particles can provide the information about the interactions between them. That idea was the basis of 'colloidal particle collider' a novel experimental technique of determining colloidal interactions [47,49].

The suitability of the creeping flow theory to the surface collisions of two uncharged spherical particles was directly confirmed by experiment by Małysa et al. who observed collisions of macroscopic spheres in silicon oil and measured their trajectories using multiple frame photography technique [54].

4. The convective diffusion theory

4.1. The continuity equation

Our considerations presented hereafter are, in principle, valid for spherical particles only because of insurmountable mathematical difficulties, no exact solutions of the continuity equation for anisotropic particle have been derived yet. However, the results obtained for spheres may be exploited as a useful reference system for colloid particles of other shapes.

Assuming that the colloid particle suspension can be treated as a stable, well-defined phase and assuming that there is no coupling between hydrodynamic and other interactions one can write the expression for the mass flux vector $\boldsymbol{j}$ in the usual form

$$\boldsymbol{j} = -\boldsymbol{D} \cdot (\nabla\mu/kT + \nabla\phi/kT)n + \boldsymbol{U}_p n \qquad (29)$$

where $\boldsymbol{D} = kT\,\mathbf{M}$ the diffusion matrix, $\mathbf{M}$ is the mobility matrix characterising all contributions stemming from the walls (described by the func-

tions F_1–F_4 as discussed previously), μ is the chemical potential of particles, ϕ the external force potential, n is the local value of particle concentration, $U_p = \mathbf{M} \cdot F_h + \mathbf{M}_r \cdot T_h$ is the particle velocity vector due to the hydrodynamic force F_h and torque T_h, and $\mathbf{M}_r$ is the rotational mobility matrix. It should be mentioned that the potential ϕ contains the contribution stemming from external sources, e.g. gravity, magnetic fields, electrostatic interactions due to the interface, etc., whereas the specific interactions between particles are contained in the chemical part of the potential μ. All these interactions have been extensively discussed in the recent review [55].

By formulating Eq. (29) all the hydrodynamic particle/particle interactions were neglected as well as all flow disturbances due to the presence of particles.

For dilute systems, as it is usually the case in the bulk of the suspension during deposition experiments, the chemical potential simply becomes $\mu = \mu_0 + kT \ln n$ (where μ_0 is some reference value of the potential). This case would correspond to the ideal bulk behaviour of the suspension. In the general case; however, e.g. in the regions where local particle concentration increases, the deviations from ideality may become significant.

For a suspension exhibiting an ideal bulk behaviour by neglecting specific and external forces, and assuming that particle velocity coincides with the fluid velocity (as is the case far from boundary surfaces) one can simplify Eq. (29) to the form [3]

$$j = -D_\infty \nabla n + Vn \tag{30}$$

where D_∞ is the diffusion coefficient in the bulk (position independent scalar quantity) and V is the unperturbed fluid velocity vector fulfilling the continuity equation $\nabla \cdot V = 0$.

Eq. (2), being the starting point of the convective diffusion theory [3] is usually referred to as the Smoluchowski–Levich (SL) approximation.

Let us now consider transport of colloid particles in the vicinity of an interface. Assume that after approaching the interface close enough, the particles become immobilized due to the presence of specific tangential interactions whose range is infinitesimal in comparison with particle dimension. Thus, upon contact, the particles do not

move along the surface although they can occasionally escape from the primary minimum region. Using the flux expression, Eq. (29) one can formulate the nonstationary continuity equation for the mobile phase as

$$\frac{\partial n}{\partial t} = -\nabla \cdot j = \nabla \cdot [(D \cdot \nabla \mu / kT + D \cdot \nabla \phi / kT - U_p)n] \tag{31}$$

where t is the time.

The mass conservation equation for the immobile phase can be formulated by observing that the increase in the surface concentration of the immobilized particles N is due to the normal component of particle flux at the interface j

$$\frac{dN}{dt} = j(\delta_m) \cdot \hat{n} = k_a n(\delta_m) - k_d N \tag{32}$$

where δ_m is the primary minimum distance [1], $\hat{n}$ is the unit normal pointing outwards from the interface and $j(\delta_m)$ is the local flux vector given by the expression

$$j(\delta_m) = (D \cdot \nabla \mu / kT + D \cdot \nabla \phi / kT - U_p)n \big|_{\delta_m} \tag{33}$$

where k_a is the adsorption rate constant characterizing the transfer rate from mobile to immobilized phase and k_d is the desorption rate constant describing particle escape rate from the immobilized phase.

Using Eqs. (32) and (33) one can formulate the general kinetic boundary condition for the bulk phase in the form

$$k_a n(\delta_m) - k_d N$$
$$= [(D \cdot \nabla \mu / kT + D \cdot \nabla \phi / kT - U_p)n] \cdot \hat{n}; \text{ at } \delta_m \tag{34}$$

Eq. (34) indicates that the bulk and surface continuity equations are coupled and cannot be solved independently in the general case. However, when one assumes the perfect sink behaviour, i.e. when the transfer rate from mobile into immobile phase k_a becomes infinite (due to the presence of infinite energy sink) and $k_d = 0$, then the boundary condition for the bulk phase assume the particularly simple form

$$n = 0 \text{ at } \delta_m \tag{35}$$

This type of boundary condition has been used in the Smoluchowski–Levich theory in conjuncture with the bulk transport equation derived by exploiting the flux expression, Eq. (30), i.e.

$$\frac{\partial n}{\partial t} = D_\infty \nabla^2 n - \boldsymbol{V} \cdot \nabla n \tag{36}$$

Later on, the PS boundary conditions, Eq. (35) have extensively been exploited in numerical calculations of particle deposition rate at various surfaces [1–6,17,18,56].

The boundary value problem expressed by the mass conservation equations, Eqs. (31) and (32) and the boundary condition, Eq. (34) is complemented by bulk boundary condition which assume usually the form

$n \to n_b$ at large distances from the interface (37)

On the other hand, for adsorption from a finite volume the symmetry boundary conditions are appropriate

$\nabla n = 0$ at the symmetry plane (38)

It should be remembered that due to presence of adsorbed particles, the chemical potential entering Eq. (31) is modified in the vicinity of the interface. One can postulate that the modified potential can be expressed as

$$\mu = \mu_0 + kT \ln(fn) = \mu_0 + kT \ln n + kT \ln f \tag{39}$$

where f is the activity coefficient which is dependent not only on the distribution and surface concentration of deposited particles but also on particle/particle interactions. Note also that f is a spatial variable having the property

$f = 1$ at distance $> 2a + \delta^*$ (40)

where δ^* is the range of particle/particle interactions.

Since the coefficient f as defined by Eq. (39) is depending on particle configuration which in turn

is determined by particle transport mechanism in the bulk (flow, diffusion, external force), both the bulk and surface continuity equations become coupled in a complicated, nonlinear way which prohibits any general solution of the boundary value problem expressed by Eqs. (31)–(35). Therefore, simplified models are usually considered like the above mentioned SL approximation Eqs. (35) and (36) or the linear model assuming an ideal behaviour in the bulk and neglecting the influence of deposited particles, when $f = 1$. In the latter case the nonstationary bulk transport equation becomes

$$\frac{\partial n}{\partial t} = \nabla \cdot [\boldsymbol{D} \cdot \nabla n + (\boldsymbol{D} \cdot \nabla \phi / kT \text{-} \boldsymbol{U}_p)\, n] \tag{41}$$

with the PS boundary conditions

A particularly attractive situation arises when the normal component of the flow and the external force are independent of coordinates tangential to the interface as is the case for the above collectors in the region close to stagnation point (or stagnation line). Then Eq. (31) can be converted into the simple one-dimensional form [57,58]

$$\frac{\partial n}{\partial t} = \frac{\partial}{\partial h}\left\{ D(h)\left[\frac{\partial n}{\partial h} + (\nabla \phi / kT)n\right] \right\} + Q(h) \tag{42}$$

where h is the separation between particle and the interface, $D(h) = F_1(H)D_\infty$, F_1 is the previously discussed hydrodynamic correction function, $D_\infty = kT/6\pi\eta a$ is the diffusion coefficient in the bulk and $Q(h) = \nabla \cdot \boldsymbol{U}_p n + \boldsymbol{U}_p \cdot \nabla n$.

Using the correction functions discussed above Eq. (42) can be formulated in the dimensionless form suitable for numerical calculations:

$$\frac{\partial \bar{n}}{\partial \tau} = \frac{\partial}{\partial H} F_1(H)\left[\frac{\partial \bar{n}}{\partial H} + \frac{\partial \bar{\phi}}{\partial H}\bar{n}\right] + \frac{1}{2} Pe\, \bar{n}\left[\frac{\partial}{\partial H}F_1(H)\, F_2(H)(H+1)^2 - 2F_3(H)(H+1)\right]$$
$$+ \frac{1}{2} F_1(H)\, F_2(H)(H+1)^2 Pe\frac{\partial \bar{n}}{\partial H} \tag{42a}$$

where $\bar{n} = n/n_b$; $\tau = t(D_\infty/a^2)$.

The advantage of Eq. (42a) (being from a mathematical viewpoint a parabolic partial differential equation) is that it can exactly be solved by standard numerical techniques, e.g. by the finite-difference Crank–Nicholson scheme [57,58] under transient (nonstationary) conditions.

Eq. (42a) can further be simplified when assuming that the steady-state conditions are established which is a valid assumption for a broad class of practically important situations when the duration of the transient regimes is of the order of seconds [59].

A number of limiting solutions to Eq. (42a) have been derived in the literature for barrier-less and barrier-controlled transport conditions as discussed below.

4.2. Limiting solutions for the perfect sink model

The solutions of quite general validity can be derived analytically for the Smoluchowski–Levich approximation. Physically, this model works best for suspensions of small colloid particles and not too vigorous flows. Then, the diffusion boundary-layer thickness remains much larger than particle dimension so the effect of specific and external force fields become negligible as well as the diffusion coefficient changes due to the presence of interfaces. The limiting solutions derived from the SL model are discussed extensively in [1–3,17,18,55]. For the collectors discussed in our work the stationary flux j_0 at the uniformly accessible region is given by

$$j_0 = C_1 \frac{D_\infty^{2/3} V_\infty^{1/3}}{R^{2/3}} n_b \tag{43}$$

where C_1 (proportionality constant) $= 0.89\, A_f$ for the sphere, $0.98\, A_f$ for the cylinder and $0.78 \alpha_s^{1/3}$ for the impinging-jet cells (where $\alpha_s(Re)$ are the dimensionless functions presented in Figs. 2 and 4), V_∞ is the characteristic velocity equal the uniform approach velocity for sphere and cylinder and Q/S for the impinging-jet cells (in the latter case R in Eq. (43) should be replaced by the capillary radius r_c or the half-width d).

Note, that this stationary value of the flux (often referred to as the limiting or initial flux) is proportional to $D_\infty^{2/3}$ rather than D_∞ as is the case for no flow conditions [3]. It is also interesting to observe that j_0 is rather insensitive to the fluid velocity V_∞.

For the region far from the stagnation point or line the stationary flux becomes position dependent and is given by the analytical formulae discussed in [3]

$$j_0 = f_s(\vartheta) \frac{D_\infty^{2/3} V_\infty^{1/3}}{R^{2/3}} Af^{1/3} n_b \tag{44}$$

where $f_s(\vartheta) = 0.78 \sin \vartheta / (\vartheta - \frac{1}{2} 2 \sin \vartheta)^{1/3}$ for sphere and

$$f_c(\vartheta) = 0.85 \frac{\sqrt{\sin \vartheta}}{\left(\int_0^\vartheta \sqrt{\sin \xi} \, d\xi \right)^{1/3}}$$

for cylinder and ϑ is the angular coordinate measured from the flow symmetry line or plane (for cylinder).

An analogous dependence of j_0 on the tangential coordinate is expected for the SIJ cell because the flow pattern is very similar as shown in Fig. 5.

It can also be deduced from Eq. (44) and the graph shown elsewhere [3] that the flux does not change appreciably for angles smaller than 90°, i.e. in the front part of the collector.

Except for predicting particle deposition rate for the initial conditions (low coverage regime), Eqs. (43) and (44) have a significance for testing the accuracy of numerical solutions of the exact continuity equation, Eq. (42a). These solutions, discussed extensively in previous reviews [1–3,55], demonstrated that the above limiting solutions can be useful for predicting deposition rate of particles smaller than 0.5 μm of diameter. For larger particle sizes, significant deviations from the Smoluchowski–Levich theory occurs as a result of the interception effect.

It was shown in [29] by performing exact numerical solutions of Eq. (42a) that the initial flux (in the uniformly accessible region) can well be approximated by the formula

$$j_0 = \frac{D_\infty}{a} \frac{1}{2} Pe\, \bar{a}^{*2} n_b \tag{45}$$

where $\bar{a}^{*2}$ is the effective particle radius which is given by [29]

$$\bar{a}^* = 1 + \frac{1}{\kappa a} \xi - \frac{2}{\kappa a} \ln\left(1 + \frac{1}{\kappa a} \xi \right) \tag{46}$$

where $\xi = \ln \dfrac{2\varepsilon a\, |\psi_1^0 \psi_2^0|}{kT\, Pe}$, κa

$\kappa^{-1} = \left(\dfrac{\varepsilon kT}{8\pi e^2 I} \right)^{1/2}$ is the Debye screening length,

ε is the dielectric constant e is the elementary charge, I the ionic strength of the electrolyte. Detailed expressions for the flux can be calculated using the Pe definitions given in Table 1.

4.3. The surface force boundary layer approximation (SFBLA)

Other analytical results of general validity can be derived in the case when an energy barrier appears due to presence of electrostatic repulsion between particles and a collector. Since these interactions are usually short-ranged in comparison with the diffusion boundary layer thickness one can use the approximate method developed originally in [60–63]. The method, referred to as the surface boundary layer approximation is based on the assumption that the particle transport through the thin surface force layer can be treated as a process independent of bulk transport. As a result, fluid convection is neglected within the surface layer of thickness δ, whereas the specific interactions are assumed negligible outside δ. We shall formulate the SFBLA in a more general form, suitable for treating the problem of the steric barrier arising due to deposited particles.

The starting point of the approach would be Eq. (29) formulated, by neglecting fluid convection in the one-dimensional form

$$j(h, t) = - D(h)\left[\frac{\mathrm{d}\ln n}{\mathrm{d}h} + \frac{\mathrm{d}\Phi/kT}{\mathrm{d}h}\right]$$
$$= - D(h)\, e^{-\Phi/kT}\frac{\mathrm{d}}{\mathrm{d}h}\, e^{\Phi/kT + \ln n} \qquad (47)$$

where the function $\Phi = \phi + kT\ln f$ can be treated as the generalized potential, f is the activity coefficient.

Considering that the relaxation time of establishing the quasi stationary transport conditions through this layer $\tau = \delta^2/D(h) \sim \delta^2/D_\infty$ is very short, one can treat j as a quasi-stationary variable, independent of time and the distance h. Then, Eq. (47) can easily be integrated within the domain $\delta_m < h < \delta$ which gives the general expression (positive flux convention used) [64]

$$j_b = \frac{n(\delta)\, e^{\Phi(\delta)/kT} - n(\delta_m)\, e^{\Phi(\delta_m)/kT}}{R_b} \qquad (48)$$

where $n(\delta_\mathrm{m})$, $n(\delta)$ is the particle concentration at the primary minimum region and at the edge of δ, respectively and

$$R_b = \int_{\delta_m}^{\delta} \frac{e^{\Phi/kT}}{D(h)}\,\mathrm{d}(h)$$
$$= \int_{\delta_m}^{\delta} \frac{e^{\Phi/kT}-1}{D(h)}\,\mathrm{d}h + \int_{\delta_m}^{\delta} \frac{\mathrm{d}h}{D(h)} = R_{exc} + R_0 \qquad (49)$$

can be treated as the static resistance due to the presence of the barrier. R_{exc} is defined as the excess resistance.

For the perfect sink model (when the interaction potential tends to minus infinity at $h = \delta$ Eq. (48) reduces to

$$j_b = \frac{n(\delta)}{R_b} = \frac{n(\delta)}{R_{exc} + R_0} = k_a^{'}\, n(\delta) \qquad (50)$$

where $k_\mathrm{a}' = 1/R_\mathrm{b}$ is the rate constant of particle deposition.

Eq. (50) can be treated as the generalized boundary condition for the bulk transport, in particular for those arising from the SL approximation.

Knowing j_b one can derive general expression for the overall flux due to barrier and bulk transport. In general, for the nonuniformly accessible surfaces this requires the bulk transport equation to be solved with the boundary conditions expressed by Eq. (50). Such solutions were derived in the case of the spherical and cylindrical collectors by Spielman and Friedlander [61] and for the parallel plate and cylindrical channel by Bowen et al. [62]. Unfortunately, explicit evaluation of the overall deposition rate as a function of parameters characterizing surface interactions can only be carried out numerically.

However, useful analytical expressions for the overall flux can be derived in the case of uniformly accessible surfaces. This can be done by exploiting the flux continuity condition $j_b = j$ (where j is the flux due to bulk transport through the macroscopic layer) from which it follows that

$$\frac{n(\delta)}{R_b} = \frac{n_b - n(\delta)}{R'_{conv}} \qquad (51)$$

where R'_{conv} is the static resistance of the diffusion boundary layer (up to the point $h = \delta$). By eliminating $n(\delta)$ from Eq. (51) one obtains the explicit expression for the overall flux in the form

$$j = n(\delta)/R_b = \frac{1}{R_b + R'_{\text{conv}}}n_b = \frac{1}{R_{\text{exc}} + R_{\text{conv}}}n_b \quad (52)$$

where $R_{\text{conv}} = R'_{\text{conv}} + R_0$ is the static resistance of the overall boundary layer in the absence of the energy barrier. R_{conv} can be estimated from previous expressions for the limiting flux since $j_0 = n_b/R_{\text{conv}}$. Using this expression one can transform Eq. (52) into the form

$$j = j_0 \frac{1}{1 + \frac{j_0}{n_b}R_{\text{exc}}} = j_0 \frac{1}{1 + \frac{j_0}{n_b}\int_{\delta_m}^{\delta} \frac{e^{\Phi/kT} - 1}{D(h)}\,dh} \quad (53)$$

The use of Eq. (53) requires evaluation of the definite integral which can be cumbersome. However, for energy profiles exhibiting well-defined maxima this integral can be evaluated analytically giving for R_b the expression [60,63]

$$R_{\text{exc}} \cong R_b \cong \left(\frac{2\pi kT}{\gamma_b}\right)^{1/2}\frac{e^{\Phi_b/kT}}{D(\delta_b)}$$
$$= \frac{a}{D_\infty}\left(\frac{2\pi\ kT}{\phi_b}\right)^{1/2} e^{\Phi_b/kT} \quad (54)$$

because

$$\gamma_b = -\left(\frac{d^2\Phi}{dh^2}\right)_{\delta_b} \sim \frac{\Phi_b/kT}{\delta^2} \text{ and } D \sim D_\infty\frac{\delta}{a}$$

For a strongly asymmetric barrier, e.g. of a triangular shape one can analogously express R_b as

$$R_b \cong \frac{a}{D_\infty}\frac{kT}{\Phi_b}e^{\Phi_b/kT} \quad (55)$$

Substituting this expression into Eq. (53) one obtains

$$j = j_0\frac{1}{1 + \frac{j_0 a}{D_\infty n_b}\frac{kT}{\Phi_b}e^{\Phi_b/kT}} = j_0\frac{1}{1 + Sh_0\frac{kT}{\Phi_b}e^{\Phi_b/kT}} \quad (56)$$

where $Sh_0 = j_0 a/D_\infty n_b$ is the dimensionless flux (Sherwood number). If $\Phi_b > 5kT$, the relative flux decreases exponentially with increasing barrier height since

$$j/j_0 \cong \frac{1}{Sh_0}\left(\frac{\Phi_b}{kT}\right)e^{-\Phi_b/kT} \quad (57)$$

The flux in the case when $f = 1$ ($\Phi = \phi$) given by Eqs. (53–56) is denoted by j'_0.

5. Non-linear deposition regimes

5.1. Surface blocking effects, the RSA and DRSA models

The linear transport conditions described by the above equations when $f = 1$ are relatively short-lasting, especially when concentrated suspensions are involved. The deviations from linearity are stemming from the presence of particles accumulated at the interface which disturb locally fluid flow and exert additional forces on adsorbing (flowing) particles. This leads to the surface blocking effect (called also surface exclusion effect) which are responsible for the reduction in particle deposition rate at higher coverage. As pointed out in [3] a rigorous theoretical analysis of these many-body phenomena seems difficult without introducing rather drastic simplifications concerning the hydrodynamic and electrostatic interactions. In the literature, these surface blocking effects are introduced, usually in the form of flux correction function $B(\Theta) = j/j'_0$ (where $\Theta = N\,S_g$ is the fractional surface coverage, N is the surface concentration and S_g is the characteristic particle cross-section area, j is the flux in the presence of particles) which depends solely on the surface coverage of deposited particles. $B(\Theta)$ is traditionally referred to as the blocking function, whereas in the physical literature a more accurate notion available surface function (ASF) is used [64,65].

The most obvious, but rather ill founded for continuous surfaces, seems the Langmuir model based on the assumption that $B(\Theta) = 1 - \Theta/\Theta_L$, where Θ_L is the 'saturation' coverage to be determined empirically. Using this function the adsorption flux j for particle covered surface is expressed as

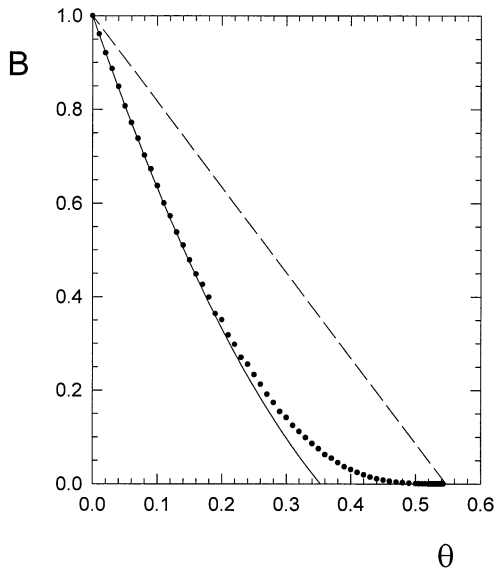$$j = j'_0\left(1 - \frac{\Theta}{\Theta_L}\right) \quad (58)$$

Fig. 9. The blocking function $B(\Theta)$ for noninteracting particles determined numerically using RSA model (points). The solid line represents the low coverage approximation calculated from Eq. (59) and the dashed line shows the Langmuirian model when $B(\Theta) = 1 - \Theta/\Theta_\infty$ ($\Theta_\infty = 0.547$).

where j_0' is the initial particle flux (discussed above).

A more realistic description of blocking effects can be attained using the random sequential adsorption (RSA) approach developed originally for hard (noninteracting) particles [64,66–73] and extended later on for interacting particles [7,74–76].

The RSA model, discussed extensively elsewhere [3], can be applied for determining the surface blocking parameter $B(\Theta)$, for modeling adsorption kinetics and for determining the maximum jamming coverages Θ_∞ (when no more particles can be put on the surface). It was found that for hard spheres and not too high surface coverages the blocking function can well be approximated by the formula

$$B(\Theta)$$
$$= 1 - 4\Theta + \frac{6\sqrt{3}}{\pi}\Theta^2 + \left(\frac{40}{\pi\sqrt{3}} - \frac{176}{3\pi^2}\right)\Theta^3 + 0(\Theta^4) \quad (59)$$

In Fig. 9 the results stemming from this equation (with the third term neglected) are compared with

exact numerical data obtained by the Monte-Carlo simulation technique. As one can observe, the above low coverage expansion works well for $\Theta < 0.3$. The jamming coverage found from these numerical simulations was 0.547. It should be noted that the Langmuir model, i.e. when $\Theta_L = \Theta_\infty$ gives poor approximation of exact date for the entire range of coverges.

The deviation from the Langmuir model becomes also pronounced for larger θ close to the jamming limit, when the blocking parameter can be approximated by the formula [70,71].

$$B(\Theta) \approx (\Theta_\infty - \Theta)^3 \quad (60)$$

One can deduce from Eq. (60) that the blocking effects predicted in the RSA model are considerably more pronounced than in the Langmuir model. This originates from the fact that due to topological constrains only a small fraction of the free surface $1 - \Theta$ is available for particle adsorption, i.e. in the later adsorption stages most of the unoccupied surface fragments (targets) are too small to accommodate additional particles [3].

Similar results as that expressed by Eqs. (59) and (60) can also be derived for interacting particle adsorption provided that the effective interaction range remains much smaller than particle dimensions [7,75,76]. Then, the many body electrostatic interactions between adsorbed and adsorbing particles can be approximated introducing the effective hard particle concept [77]. It was demonstrated that in this case the low coverage expansion for $B(\Theta)$ assumes the form

$$B(\Theta) = 4(1 + H^*)^2\Theta + \frac{6\sqrt{3}}{\pi}(1 + H^*)^4\Theta^2$$
$$+ \left(\frac{40}{\pi\sqrt{3}} - \frac{176}{3\pi^2}\right)(1 + H^*)^6\Theta^3 \quad (61)$$

where $H^* = h^*/a$ is the effective interaction range given by the expression [76]

$$H^* = (\kappa a)^{-1} \ln \phi_0/\phi_{\text{ch}} \quad (62)$$

where $\phi_0 = \varepsilon a(kT/e)^2 \bar{Y}_1^{0^2}$, $Y_1^0 = 4 \tanh(eY_1^0/(4kT))$ is the effective potential of the particle and ϕ_{ch} is the characteristic energy close to one kT unit [76].

It was also demonstrated that the jamming coverage for interacting particles is given by the

simple expression (referred to as the maximum coverage Θ_{mx})

$$\Theta_{mx} = \frac{\Theta_{\infty}}{(1 + H^*)^2} \quad (63)$$

The dependence of H^* on the κa parameter determined numerically for spheres and spheroids is plotted in Fig. 10. As can be observed Eq. (62) is a good approximation for the entire range of κa.

It should be mentioned that the blocking effects in the Langmuir and RSA models discussed above are treated as purely surface phenomena. In reality, due to finite particle size, the blocking effects are extending into the bulk of the particle suspension over the distance comparable with particle diameter. This leads to a change in particle chemical potential as described by Eq. (39). Physically, this effect can be interpreted as if an energy barrier (Θ, h) $\phi_s = kT \ln f\phi_s$ was formed (sometimes referred to as the steric barrier [55]) whose magnitude is growing with particle coverage. The
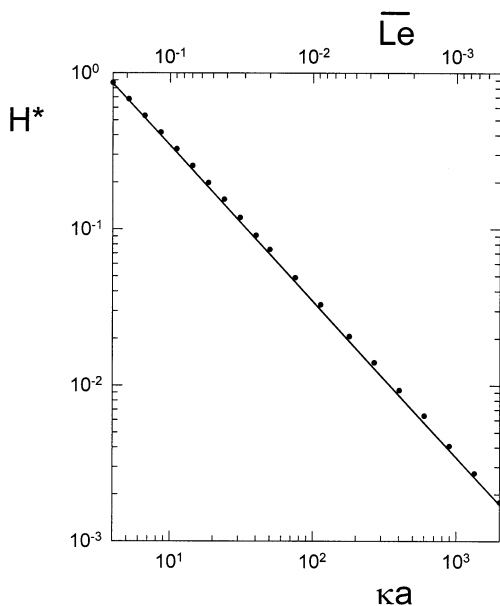

Fig. 10. The dependence of the effective interaction range H^* on the κa $(\overline{Le} = 1/\kappa a)$ parameter [76]. The points represent exact numerical results obtained from numerical simulation performed according to the RSA model and the continuous line shows the represents the analytical results calculated from Eq. (62).

height of barrier at the interface ϕ_s^0 equals $- kT \ln B(\Theta)$ and it vanishes for distances exceeding the effective particle diameter. Analogously as for the electrostatic interactions, the influence of this barrier on particle transport can be analysed in terms of the SFBLA. In this way the following general expression describing particle flux was derived [65]

$$\frac{j(\Theta)}{j_\delta} = \bar{B}(\Theta)$$

$$= \frac{\displaystyle\int_{\delta_m}^{\delta} \frac{e^{\phi/kT}}{D(h)} \, dh}{\displaystyle\int_{\delta_m}^{\delta} \frac{e^{\phi/kT} \, dh}{D(h)} + \int_{\delta_m}^{\delta} [e^{\phi_s(\Theta, h)/kT} - 1] \frac{e^{\phi/kT}}{D(h)} \, dh} \quad (64)$$

where j_δ is the flux through the layer of thickness in absence of the steric barrier and $\bar{B}(\Theta)$ is the generalised blocking function.

It is difficult to evaluate $\bar{B}(\Theta)$ explicitly because ϕ_s is dependent not only on particle coverage but also on particle distribution over the surface. However, it was demonstrated in [65] that the differences between this generalised approach (referred to as the DRSA model) and the usual RSA model discussed above are not too significant for small and moderate surface coverages except for the case of dense particles sedimentating to the interface. Then, the so called ballistic model becomes more appropriate [78]. For higher surface coverages no exact results for $\bar{B}(\Theta)$ were reported although it was demonstrated that the jamming limit is the same as for the classical RSA model [79].

Eq. (64) describes the transport through the layer of thickness δ (equal to the effective particle size) where the fluid convection is neglected. In practice, for protein and colloid suspensions, δ is very small in comparison with the overall diffusion boundary layer thickness where the convection or external force dominate. In order to derive equations characterising the overall transport rate one can use the SFBL concept by postulating that the overall transport resistance is a sum of the steric resistance $1/\bar{B}(\Theta)$ governed by and the bulk resistance R_{conv}. Then, using Eq. (53) one can formulate the expression for the flux in the presence of deposited particle in the form

$$\frac{j(\Theta)}{j_0'} = \tilde{B}(\Theta) = \frac{Ka}{Ka - 1 + \dfrac{1}{\bar{B}(\Theta)}} \quad (65)$$

where

$$Ka = \frac{1}{\bar{j}_0 \displaystyle\int_{\delta_m}^{\delta} \frac{e^{\phi/\mathrm{KT}}}{D(h)}\, dh} \quad (66)$$

where $\bar{j}_0$ is the reduced initial flux discussed previously and $\tilde{B}(\Theta)$ is the overall blocking function.

When Ka assumes values much larger than unity (as is the case for protein and colloid particle transport) Eq. (65) simplifies to

$$\tilde{B}(\Theta) = 1 - \left(\frac{1}{\bar{B}(\Theta)} - 1\right)/Ka$$

$$\cong 1 - \left(\frac{1}{\mathrm{B}(\Theta)} - 1\right)/Ka \quad (67)$$

Eqs. (65)–(67) indicate that in the influence of the surface blocking effects on particle adsorption rate will be negligible as long as the inequality $Ka \gg 1/\bar{B}(\Theta)$ holds.

However, the surface blocking effects always become important when surface coverage approaches the jamming (or maximum) values Θ_{mx} because $1/\bar{B}(\Theta) \to \infty$ and

$$\frac{j}{n_b} \cong \bar{j}_0 Ka\ \bar{B}(\Theta) = \frac{1}{\displaystyle\int_{\delta_m}^{\delta} \frac{e^{\phi_s(\Theta,h)/kT}\, e^{\phi/kT}}{D(h)}\, dh} \quad (68)$$

It is not possible to evaluate this integral in a general case because the dependence of the steric barrier $\phi_s(\Theta, h)$ on the distance is not known for higher coverages. However, noting that the steric barrier is the highest at primary minimum one can use the SFBLA to show that particle flux can be approximated by the expression

$$\frac{j}{n_b} = C_s B(\Theta) \quad (69)$$

where the dimensionless constant C_s of the order of unity can be assumed fairly independent of coverage [55].

The RSA models discussed in this section are expected to describe adequately deposition of sub-micrometer sized particles for which the diffusional transport dominates at distances comparable with particle diameter and when there is no coupling between the specific and hydrodynamic force fields. For larger particles the hydrodynamic flow penetrates the surface layer and a significant coupling between the electrostatic and hydrodynamic force fields occurs. This is leading to the hydrodynamic scattering effect (HSE) enhancing the surface blocking phenomena as disscussed below.

5.2. The hydrodynamic blocking

As previously demonstrated (See Figs. 7 and 8) particle trajectories in the vicinity of an attached particle become highly asymmetric due to the presence of short-range repulsive interactions (due to, e.g. roughness of the particle surface or electrostatic interactions). As a result, the probability of particle deposition behind the attached particle is strongly reduced over distances exceeding particle dimension. The size and shape of the hydrodynamic 'shadow' is also dependent on particle/wall specific interactions and Brownian motion of particles which makes a quantitative analysis of this problem prohibitive. However, useful approximations can be derived by exploiting the stochastic trajectory analysis presented in [43,80]. Typical results obtained from these simulations for a 1 μm of diameter particle immersed in the plane-parallel stagnation flow (corresponding to the SIJ cell discussed above) are shown in Fig. 11. The density of the points is proportional to the adsorption probability of the flowing particle in the vicinity of an attached one. Qualitatively, it can be observed that the width of the shadow increases with the double-layer thickness (characterised by the κa parameter), whereas its length seems independent of this parameter. Detailed numerical studies of this effect performed in [43] for the case of plane-parallel stagnation flow enabled one to formulate the following equation describing the geometrical area of the shadow

$$\bar{S}_1^* = \frac{S_1^*}{\pi a^2} = 4(1 + H^*)^2 + C_h(1 + H^*)Pe^n\frac{x}{a} \quad (70)$$

where Pe, is the previously defined Peclet number and C_h, n are the dimensionless fitting parameters which have to be determined by simulations.
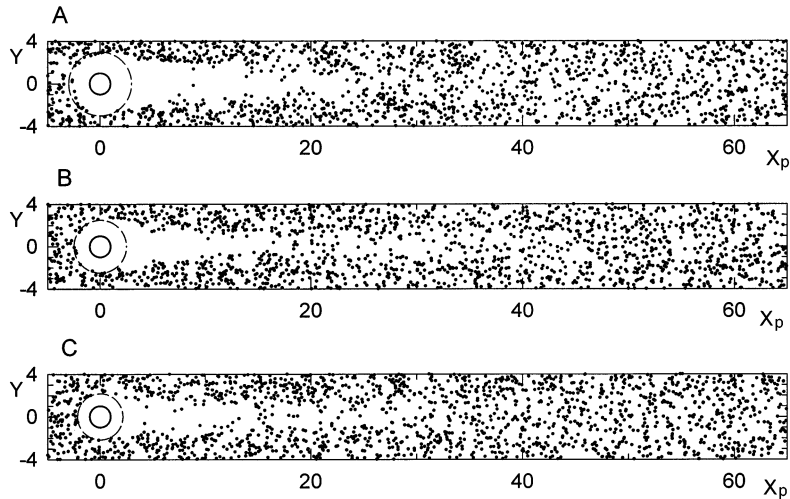
Fig. 11. The simulated Brownian electro-hydrodynamic shadow behind the particle attached to the interface in the stagnation line flow for $Pe = 0.1$, $x/a = 315$. Part A for $\kappa a = 7$, B for $\kappa a = 16$ and C for $\kappa a = 50$. Solid circle represents the contour of the attached particle, dashed circle is the area blocked by the charged particle in absence of flow.

These results are directly applicable for the SIJ cell and cylinder in simple shear at distances not too far from the symmetry plane. Although numerical simulations were not reported, it seems that Eq. (70) is also applicable for the stagnation point flow, i.e. for the sphere in uniform flow and the SIJ cell in the vicinity of the symmetry point. However, at larger distances from the stagnation point (or stagnation plane in the case of the cylinder) the perpendicular velocity component vanishes and the flow around the sphere and cylinder becomes similar to the simple shear flow as discussed previously. The same is valid for the SIJ and RIJ cells at dimensionless distances larger than 0.5 (cf. Fig. 5). A dimensional analysis would suggest that in this case $n = 1$, although no numerical results were reported. It can also be predicted that this hydrodynamic blocking effect (referred also to as the hydrodynamic scattering effect HSE) should be the largest in the region close to the rear of the spherical and cylindrical collectors because the perpendicular fluid velocity component is directed outwards from the surface. However, the flux in this region is already very small so the HSE will be difficult to observe.

Knowing the dimensionless surface area blocked by one particle S_1^* one can apply the RSA analysis for predicting blocking effects as a function of Θ which results in the following expansion [9]

$$\frac{j}{j_0} = B(\Theta) \cong 1 - C_{1h}\Theta + C_{2h}\Theta^2 \tag{71}$$

where $C_{1h} = \bar{S}_1^*$ and $C_{2h} = qC_{1h}^2$, q is the dimensionless geometrical constant equal to $1/8$ in the case when the real shape of the shadow is approximated by a rectangle [9]. Due to mathematical difficulties and limited accuracy of the expression for S_1^*, only two terms of the expansion were specified.

From Eq. (71) one can deduce that the 'apparent' saturation coverage Θ_S (when $B = 0$) equals

$$\Theta_s = \frac{C_{1h}}{2C_{2h}}\left[1 - \sqrt{1 - \frac{4C_{2h}}{C_{1h}^2}}\right] = \frac{1 - \sqrt{1 - 4q}}{2q}$$

$$\frac{1}{(1 + H^*)\left[4\,(1 + H^*) + C_{1h}Pe^n\dfrac{x}{a}\right]} \tag{72}$$

One can deduce from the above relationship that in the case when the product $Pe^n(x/a)$ assumes large values (particle size above micrometer and intense flows) the saturation coverage becomes much smaller than unity and is given by the asymptotic formula

$$\Theta_s \sim \frac{1}{C_{1h}(1 + H^*)Pe^n \frac{x}{a}} \sim \frac{1}{[\alpha_s(Re)Re]^n a^{4n-1} x} \quad (73)$$

This equation suggests, contrary to intuition, that the increase in flow rate (*Re* number) will result in a considerable decrease in the amount of particle deposited under steady-state conditions. The effect is expected to play a more significant role for simple shear flows ($n = 1$) when the perpendicular component of fluid velocity vanishes.

Although the above analytical results are of limited accuracy they seem to reflect the most important features of hydrodynamically driven blocking. These equations are significantly more convenient for estimations of large particle deposition kinetics than the cumbersome Brownian Dynamic simulations [3]

6. Experimental results

6.1. Experimental method — general remarks

The literature concerning experimental measurements of colloid particle deposition at solid/liquid interfaces is fairly extensive and has been reviewed in some detail in our previous reviews [1–3,55] and books [17,18]. In this paper we present some selected experimental results obtained under well-defined transport conditions which elucidate the decisive role of the coupling between hydrodynamic and specific force interactions in particle deposition processes.

There exists a large variety of experimental methods aimed at a quantitative determination of colloid particle adsorption kinetics either indirect or direct as discussed in [3]. The simplest to implement are the indirect methods when the suspension concentration changes in the bulk are measured prior and after contact with the adsorbent (interface). The depletion of the solute concentration is often determined by turbidimetry [81], interferometry or nephelometry [82] or by applying the HPLC and FPLC methods coupled with appropriate detecting system [83,84]. Sometimes fluorescent [85] or radioactive [86] labeling of the adsorbate is used. Another class of indirect

methods is based on measurements of the signal stemming from the adsorbed particles, as is the case in ellipsometry [11], reflectometry [12–15] radioactive labeling [87–91] or streaming potential measurements [92–95]. The disadvantage of these methods is that one can usually gain a global information averaged from a considerable surface area of the interface. As an results, any detailed information about the local structure of the mono-layer (e.g. density fluctuations or inhomogeneities) is not available.

It seems that an unequivocal determination of particle adsorption kinetics and structure of adsorbed layers can only be achieved using the direct methods based on optical, AFM or electron microscope observations. For suspensions of larger sized colloids or bacteria the number of particle adsorbed can be determined in situ, in a continuous manner using the optical microscopy coupled with a micrograph [6–9] or image analysis techniques [10,96,97]. Usually, the well-defined transport conditions are realized using the above described impinging-jet cells. Recently, the AFM tapping mode was used for direct in situ imaging of latex particle (diameter 0.116 μm) adsorbed on mica [98,99]. However, the use of this technique awkward due to artifacts stemming from tip-induced aggregation of the suspension, convolution of the tip and particle signal, adhesion of particles to the tip etc. A considerably better resolution can be achieved by imaging the particle in the air upon drying the sample. In this case the size of individual adsorbed particles can be determined with a high accuracy [99]. However, the drying procedure is a rather invasive technique leading to distortion of particle structure or removal of particles from the surface.

Due to reliability of the direct methods they seem to be the most appropriate for a quantitative verification of theoretical predictions, especially those concerning initial deposition rate when the surface coverage remains of the order of a percent.

6.2. The initial deposition rates

The occurrence of the linear deposition regimes under barrier-less transport conditions in experi-

ments involving colloid particles was often demonstrated [1–3,55]. The quantity which was measured directly in these experiments was the number of particles N_p found over equal-sized surface areas ΔS selected at random at a fixed distance from the cell center [9]. Then, the averaged value of $<N_p>$ is determined which can be used for calculating particle flux from the equation

$$\bar{j}_0 = \frac{j_0}{n_b} = \frac{\Delta\langle N_p\rangle}{n_b\Delta S\Delta t} = \frac{1}{\pi a^2}\frac{\Delta\Theta}{n_b\Delta t} \qquad (74)$$

where $\Delta<N_p>$ is the change in the averaged number of particles adsorbed over ΔS within the time interval Δt (after a given adsorption time t). In order to increase the accuracy of $\bar{j}_0$ determination averages from many experiments with different n_b are taken and the nonlinear curve fitting procedure is applied [9]. The relatively high accuracy of the initial flux measurements can be ex-

ploited for determining applicability of the convective diffusion theory, in particular the Smoluchowski–Levich approximation.

Typical results obtained in the RIJ cell using mono-disperse polystyrene latex suspensions of negatively charged particles are shown in Fig. 12. Particle deposition occurred at modified mica surface (positively charged) which assured localized and irreversible adsorption conditions. The ionic strength in these experiments was kept relatively high (10^{-3} M) in order to eliminate the electrostatic interactions. The results shown in Fig. 12 suggest that for particles having size below 1 μm, $\bar{j}_0$ can well be reflected by the Smoluchowski–Levich approximation given by Eq. (43), predicting that the initial flux decreases with particle size according to $a^{-2/3}$. This indicates that the diffusion and convection were the dominating transport mechanisms.

On the other hand, for particle sizes above 1 μm the interception effect described by Eq. (45) was playing an increasingly important role, especially for higher flow rates ($Re = 150$). This causes a considerable (manyfold) increase of the initial flux over Levich's theory predictions. It should also be noted that the numerical solutions of the exact transport equation, Eq. (42a) reflect well with the experimental data for the entire range of particle sizes studied.

Since according to Eq. (45) the interception effect should increases parabolically with the effective particle size, one may expect that electrostatic interactions should play a significant role in particle deposition at initial stages. This effect is illustrated in Fig. 13 where the results obtained in the RIJ cell using mono-disperse latex suspension (averaged particle diameter 0.68 μm) are presented. As one can notice, for $I > 10^{-3}$ M, the electrostatic interactions seem to be effectively eliminated since the limiting flux $\bar{j}_0$ attains a plateau value for all Re number studied (8–150). This confirms that the results shown previously in Fig. 12 can be treated as the limiting values, characteristic for hard particles. On the other hand, for decreasing ionic strength, the limiting flux is enhanced considerably over the hard particle values (for $Re = 150$ this increase is about four times). It should be observed that the flux increase
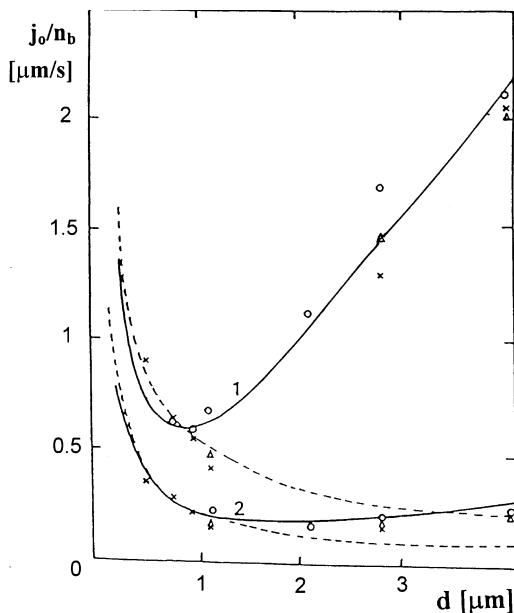

Fig. 12. The dependence of the reduced initial flux $\bar{j}_0 = j_0/n_b$ on particle diameter d. The points show the experimental results obtained in the RIJ cell at $I = 10^{-3}$ M using various monodisperse latex suspensions [6]. The solid lines are the exact numerical solutions of the convective diffusion equation and the broken lines show the data calculated using the Smoluchowski–Levich approximation (Eq. (43)). 1: $Re = 150$ 2: $Re = 30$.
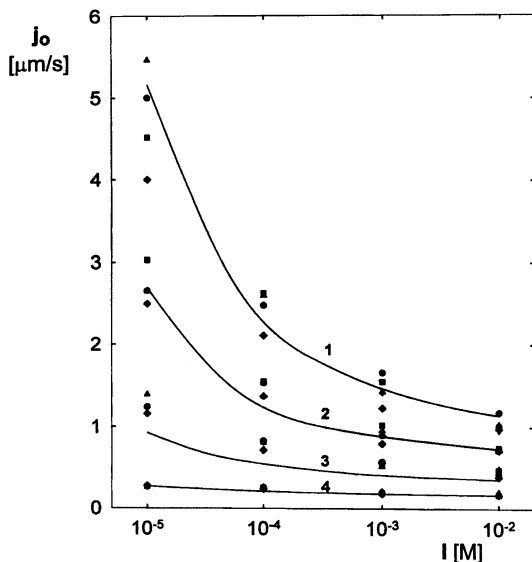
Fig. 13. The dependence of the reduced flux $\bar{j}_0 = j_0/n_b$ on the ionic strength of the latex suspension regulated by addition of various electrolytes. The points denote the experimental data obtained in the RIJ cell for various electrolytes, i.e. KCl, CsCl, LiCl, BaCl$_2$, K$_2$SO$_4$ latex particles ($d = 0.68$ μm adsorbing at mica). 1: $Re = 150$; 2: $Re = 80$; 3: $Re = 28$; 4: $Re = 8$; the continuous lines show the theoretical results obtained from exact numerical solution of the convective diffusion equation (Eq. (42)).

remains fairly independent (within experimental error bounds) of the kind of electrolyte used, i.e. KCl, CsCl, LiCl, BaCl$_2$ and K$_2$SO$_4$ (at equal ionic strength). Thus, the flux enhancement for larger particle size and the indifference to electrolyte composition is in a good agreement with the effective hard particle concept described by Eqs. (45) and (46). Note also that the numerical results (continuous lines in Fig. 13) are in a quantitative agreement with the experimental data for the entire range of ionic strength investigated.

The increase in the initial flux in dilute electrolyte solutions due to the interception effect is an universal phenomenon occurring for other flow configurations more related to practice, e.g. for the spherical collector discussed above. This was demonstrated by Elimelech [100] who carried out a series of throughout experiments on particle deposition (filtration) in columns packed with glass beads. The suspensions used were positively charged latex particles of various size ranging

from 0.08 to 2.51 μm with the ionic strength varied between 5×10^{-6} M (deionized water) to 0.1 M. The number of particles adsorbed was determined indirectly (depletion method) by monitoring the optical density change at the outlet of the column. It was found that the increase in the initial particle flux was larger than four times when using deionized water. This effect was quantitatively interpreted in terms of the numerical solutions of the continuity equation discussed above. Similar results were obtained for larger particle sizes although the measured particle deposition rates were generally smaller than predicted theoretically [100]. This deviation can probably be explained by the hydrodynamic scattering effect which may occur at surface coverages as low as a few per cent, affecting therefore the initial flux determination. This is discussed in more detail later on.

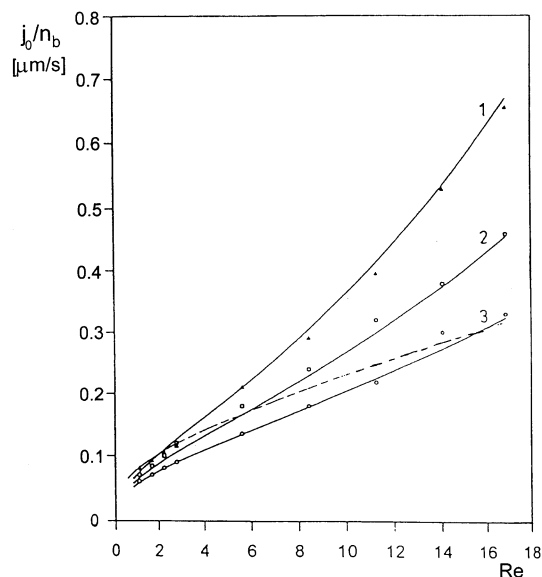Other data confirming the significant role of attractive double-layer interactions in particle de-

Fig. 14. The normalized particle flux j_0/n_b vs. the Reynolds number Re determined experimentally for the monodisperse latex suspension ($d = 1.48$ μm) in the slot impinging-jet cell for various ionic strength. 1: $I = 2 \times 10^{-5}$ M; 2: $I = 10^{-4}$ M and 3: $I = 10^{-3}$ M. The solid lines denote the theoretical results obtained from numerical solution of transport equation, the dashed line shows the results of the Smoluchowski–Levich approximation.
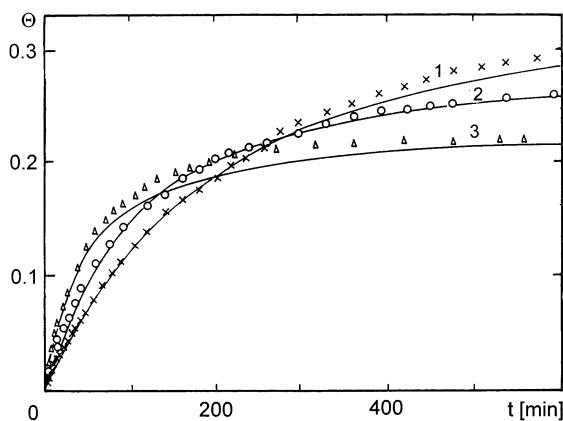
Fig. 15. Adsorption kinetics of 0.94 μm latex particles on silanized mica measured in the centre of the slot impinging-jet cell for $Re = 8$, $n_b = 4.4 \times 10^8$ cm^{-3} in 1: 10^{-3} M; 2: 10^{-4} M and 3: 1.2×10^{-5} M KCl. Solid lines represent the RSA simulations.

position phenomena are presented in Fig. 14. These results were obtained in the SIJ cell using a mono-disperse latex suspension (averaged particle size 1.48 μm) [10]. As can be observed the agreement between the experimental and theoretical data is satisfactory for the entire range or Re number studied. It should be noted that for $Re < 4$ (which corresponds to $Pe < 10^{-2}$) the experimental results approach the same limiting curve which suggests that for low Reynolds number flows the attractive electrostatic interactions exert negligible effect on particle deposition rate. It should be noted, however, that even at such low Re number the experimental results and the theoretical predictions are well below the Smoluchowski–Levich predictions (depicted by the broken line in Fig. 14). This deviation can be explained by the sedimentation of particles outwards from the surface (the specific particle density was 1.05 g cm^{-3}) and partially by the increased hydrodynamic resistance of particle moving perpendicularly to a wall (cf. Fig. 6). On the other hand, for increased Re number the measured flux values exceed manyfold these stemming from the Smoluchowski–Levich theory which is a spectacular manifestation of the coupling between hydrodynamic and electrostatic force fields.

The above presented results and others discussed elsewhere [1–3,55] seem to confirmed quantitatively the validity of the convective diffusion theory for predicting deposition kinetics of arbitrary sized particles. However, these results are valid for limiting range of surface coverage only, because for higher coverages, the blocking effects dominate as discussed below.

6.3. Non-linear adsorption kinetics

Most of the experimental results presented hereafter were obtained in the stagnation flow cells for micrometer sized particles with gravity acting opposite to the interface. Under such circumstances one can expect that the surface blocking effects can well be characterised by the RSA model, especially for moderate Re number when the diffusion boundary layer thickness remains comparable with particle diameter and the HSE is not too important. Typical kinetic curves measured under these circumstances for various ionic strength are shown in Fig. 15 (the SIJ cell, averaged particle size 0.94 μm, $Re = 8$, bulk suspension concentration $n_b = 4.4 \times 10^8$ cm^{-3} [10]).

One can observe that for initial deposition stages (for coverage $\Theta < 0.1$) the slope of the kinetic curves (particle flux) decreases with ionic strength in accordance with previous discussion (see Fig. 13). On the other hand, for longer adsorption times an opposite trend is observed, since the adsorption flux (the slope of the Θ vs. time dependence) is the smallest for the lowest ionic strength, i.e. $I = 1.2 \times 10^{-5}$ M. In the latter case the flux becomes practically negligible after reaching the surface coverage of 0.26. It is also interesting to observe that the experimental data shown in Fig. 15 can well be accounted for by the RSA model with the blocking function $B(\Theta) = 1 - C_1\Theta + C_2\Theta^2$. The kinetic curves were obtained by integrating this relationship in respect to time which resulted in the equation

$$\Theta = \Theta_1 \frac{1 - e^{-pC_1 t/t_{ch}}}{1 - \dfrac{\Theta_1}{\Theta_2} e^{-pC_1 t/t_{ch}}} \tag{75}$$

where $t_{ch} = 1/\pi a^2 \bar{j_0} n_b$.

$$\Theta_1 = \frac{C_1}{2C_2}(1-p), \ \Theta_2 = \frac{C_1}{2C_2}(1+p), \ p$$

$$= \left(1 - \frac{4C_2}{C_1^2}\right)^{1/2}, \ \frac{4C_2}{C_1^2} > 0$$

$\bar{j}_0$ is the initial flux determined from exact solution of the transport equation. The results shown in Fig. 15 demonstrate unequivocally that the coverage attained after longer adsorption time are considerably increased for higher electrolyte concentration. It should be mentioned that analogous trends were observed in the kinetic measurements of Johnson and Lenhoff [98] performed by the AFM method using the amidine latex particles (mean diameter 0.116 μm) adsorbing at freshly cleaved mica. Similarly, Johnson and Elimelech [101] demonstrated that the kinetic breakthrough curves of packed bed columns depend significantly on the suspension ionic strength in accordance with the RSA model discussed above. The commonly used Langmuir model was proven inaccurate in this case.

Further evidences of the validity of the RSA model for characterising protein adsorption were reported by Ramsden [102].

The good agreement of the experimental data shown in Fig. 15 and the data reported by Johnson and Elimelech [101] with the classical RSA model is probably caused by the fact that the diffusion boundary layer thickness was comparable with particle diameter, hence the dimensionless constant Ka was close to unity. Under such circumstances the overall blocking function $\tilde{B}(\theta)$ can be expressed according to Eq. (65) as

$$\tilde{B}(\theta) = Ka \ \bar{B}(\theta) \tag{76}$$

As $\bar{B}(\theta)$ stemming from the DRSA model is slightly smaller the $B(\theta)$ calculated from the RSA model and Ka is slightly larger than unity the product of the quantities can be close to the blocking function of the classical RSA model, given by Eqs. (59) and (60).

However, for lower Re flows or for small particles, e.g. proteins, the value of Ka becomes much larger than unity and the above discussed coupling of the bulk and surface transport becomes important as predicted by Eq. (65). No quantitative results for this case were reported in the

literature although the recent data of Bohmer et al [14] and Semmler et al [99] obtained by reflectometry and the AFM technique would suggest that this equation is valid. It seems that further, more precise experiments are needed for a unambiguous determination of deposition kinetics under diffusion-controlled regime and for assessing the range of validity of the RSA and DRSA models in these processes.

From practical viewpoint, a more interesting then these subtle differences in deposition kinetics, is the maximum coverage Θ_{mx} attained after longer deposition times. As can be deduced from Eqs. (62) and (63), this quantity is considerably affected by the ionic strength of the suspension. Many experiments were reported in the literature aimed at determining Θ_∞ as a function of ionic strength and particle size. The mono-layer density was determined mostly using the direct methods based on electron microscope AFM or optical microscope counting of adsorbed particles. These data discussed extensively in the recent review [55] proved that the classical RSA model with the modification for the effective interaction range as described by Eq. (63) works well for $\kappa a > 2$. In accordance with this equation it was found that for $\kappa a = 10$ the maximum coverage Θ_{mx} is almost two times smaller than the maximum jamming limit for hard spheres Θ_∞ (= 0.547 as previously stated). For $\kappa a = 100$ the deviation is of the order of 2 percent.

6.4. The hydrodynamic scattering effect

All these results were obtained under conditions when diffusion was the predominant transport mechanism, hence the HSE was not operating. However, as mentioned above, for larger particles and higher Re flows, the hydrodynamic blocking effects should decisively influence deposition kinetics and the maximum coverages as predicted by Eq. (72). This can be observed in Fig. 16 where the data obtained in the SIJ for 1.48 μm of diameter latex particles are plotted [10]. Particle deposition was measured at the distance of 158 μm from the cell symmetry plane so the product $Pe^n(x/a)$ was relatively high, i.e. 3.2 for $Re = 2$, 31 for $Re = 8$ and 90 for $Re = 16$. One can notice

that the increase in flow rate diminished significantly particle deposition rate at longer times. Accordingly, the apparent saturation coverage decreased monotonically with the flow rate attaining values as low as 4% for $Re = 16$. It should be
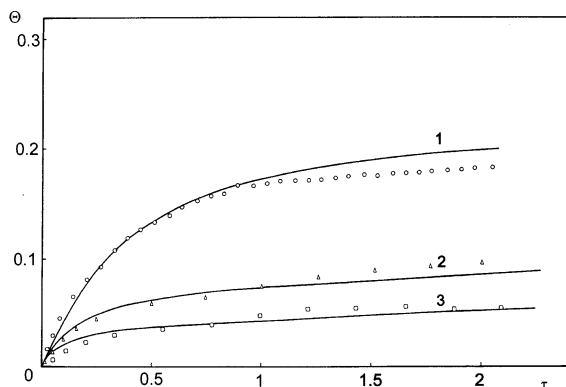

Fig. 16. Adsorption kinetics of the latex particles ($d = 1.48$ μm) expressed as the dependence of Θ (measured at the distance of 158 μm from the cell centre) on the dimensionless adsorption time τ ($I = 10^{-4}$ M); the points show experimental results obtained for (1) $Re = 2$; (2) $Re = 8$ and (3) $Re = 16$. The solid lines represent the SBD simulations.
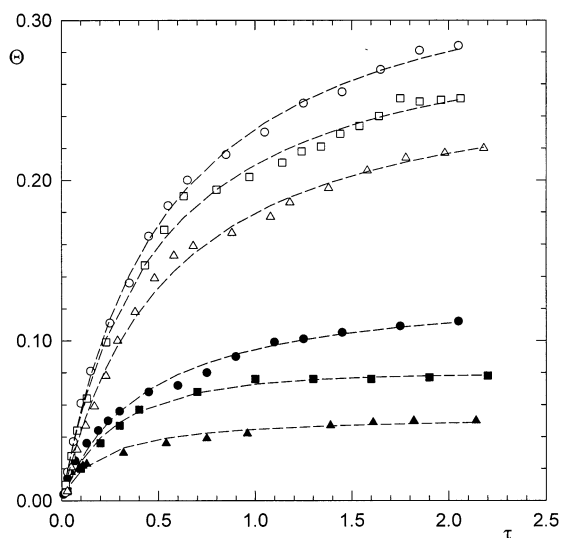

Fig. 17. Adsorption kinetics of latex particles ($d = 1$ μm) at silanized mica observed in the slot impinging-jet cell at the distance of 158 μm from the centre for $Re = 2$ (empty symbols) and $Re = 16$ (filled symbols). Triangles $I = 2 \times 10^{-5}$ M, squares $I = 10^{-4}$ M and circles $I = 10^{-3}$ M KCl. Lines represent results calculated from Eq. (75) with Θ_s given by Eq. (72).

noted that the kinetic curves can well be reflected for the entire range of dimenionless time $\tau = t/t_{ch}$ by the theoretical results (continuous curves) derived from numerical simulations (Brownian Dynamics method described in [3]). Also, the approximate analytical results calculated from Eq. (75) (with the $C_1 = C_{12}$, $C_2 = C_{22}$ seem to be in a good agreement with the experimental data. This conclusion is further confirmed by the results presented in Fig. 17 where the influence of ionic strength on particle deposition kinetics is shown (SIJ cell, latex particles 1 μm of diameter, distance 158 μm from the cell center). As can be observed, the increase in the ionic strength exerted an opposite effect on particle deposition kinetics which was the slowest for $Re = 16$ and ionic strength of 2×10^{-5} M. In this case the apparent saturation coverage was less than 5%. One can observe again that the analytical dependence, Eq. (75) describes well experimental data predicting also properly the apparent saturation coverage Θ_s given by Eq. (72). One may deduce, therefore, from the data shown in Figs. 16 and 17 that the hydrodynamic scattering effect is the decisive factor in deposition phenomena of micrometer sized particles, especially at lower ionic strength.

Another important manifestation of the HSE is that the apparent saturation coverage Θ_s should depend on the dimensionless distance from the cell center. This prediction was confirmed by experimental measurements in the SIJ cell using the 1 μm of diameter latex particles. As can be seen in Fig. 18 the saturation coverage decreases monotonically with the distance from the cell center x/a in a quantitative agreement with the theoretical predictions stemming from Eq. (72). Since the flow distribution in the SIJ cell is very similar to the cylindrical collector (see Fig. 3) one may expect that the results presented in Fig. 18 can be used for predicting the saturation coverage distribution over the cylinder surface.

It should be emphasised that the saturation coverages observed for long adsorption times and larger distances far from the cell center are not the equilibrium or jamming coverages since particle adsorption was irreversible and only a small fraction of the interface was covered. The apparent saturation of the surface is a purely kinetic due to
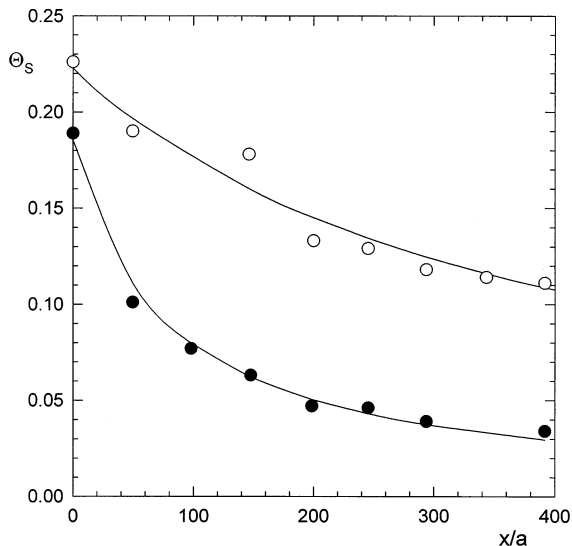
Fig. 18. The quasi-saturation coverage Θ_s of the monodisperse latex particles ($d = 1.48$ μm) at silanized mica as a function of distance from the stagnation line x/a. Empty symbols $Re = 2$ ($Pe = 0.05$), filled symbols $Re = 16$ ($Pe = 1.1$).
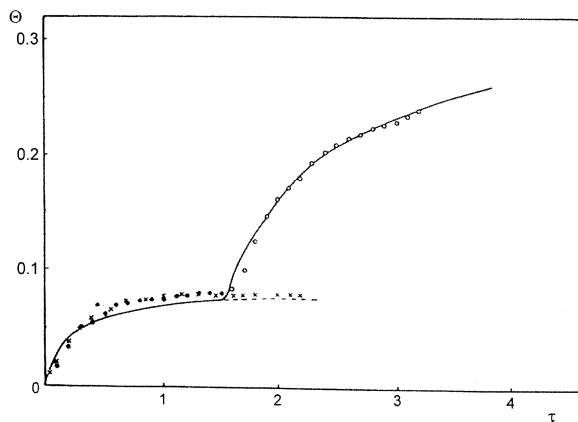

Fig. 19. Adsorption kinetics of latex particles ($d = 1$ μm) at silanized mica determined for $x = 158$ μm ($I = 10^{-4}$ M). The filled circles show results of a composite experiment when at the time $\tau = 1.6$ ($t = 455$ min) the Reynolds number was decreased from $Re = 16$ (initially) to $Re = 2$. The crosses show the results of a simple experiment when the flow rate remained constant. The solid line represents the SBD simulations.

the HSE. This was unequivocally demonstrated in [9,10] by performing a 'composite' kinetic measurement. At the beginning particle adsorption was carried out for flow rate corresponding to Re number $= 16$ until the apparent saturation cover-

age was reached (see Fig. 19) Then, for $\tau = 1.6$ the flow rate was decreased eight times (to $Re = 2$). This promoted further particle adsorption until a new saturation coverage was reached, almost three times higher that the previous one. Note that also in this case the numerical simulations are in a good agreement with experimental data.

Although the mean features of the hydrodynamically driven blocking were quantitatively confirmed in the above discussed experiments there is still need for additional experiments to be performed for other flow configuration, especially for the simple shear.

7. Conclusions

It was theoretically demonstrated that the flow pattern in the RIJ and SIJ cells matches closely the flow in the vicinity of the spherical and cylindrical collector, respectively. This concerns both isolated collectors as well as those forming a structured layer, like the packed bed or filtration mat. Hence, the experimental results obtained in these cells can quantitatively be transferred to these more complicated collector geometry, difficult to study in a direct way.

The analysis of available experimental data obtained using these cells showed that for submicrometer sized particles the initial deposition flux can well be described by the Smoluchowski–Levich approximation neglecting the interception, external force, and hydrodynamic wall effects. For this particle range the specific interactions may exert an influence on particle transport when forming a potential barrier only. Then, the initial flux can be predicted from the SFBLA, i.e. from Eq. (53). The concept of the potential barrier can also be used for describing the blocking effects due to the presence of deposited particles. It was predicted, however, that in the case when the thickness of the diffusion boundary layer exceeds considerably particle diameter (small particles, low Re flows) the influence of blocking effects remains negligible until the maximum coverages Θ_{mx} are approached. These limiting coverages can be calculated from Eq. (63) derived by exploiting the effective hard particle concept.

For particle size approaching micrometer and above the Smoluchowski–Levich approximation fails due to increasing role of the interception effect enhanced by attractive electrostatic interactions and external forces (gravity). In this case j_0 can only be determined in an exact manner by numerical solutions of the rigorous transport equation. Approximate results for the interception effect can, however, be derived from Eq. (45) which shows that the initial flux is significantly increased for low ionic strength suspensions (inverse salt effect).

For this particle range the blocking effects due to adsorbed particles play a significant role already for low coverages. When the local shear rate is small these blocking effects can well be approximated by the RSA model with the modification for the effective particle size. As a result, for higher coverage and low ionic strength, particle flux is considerably reduced due to increased lateral repulsion among deposited and flowing particles.

For larger shear rates the blocking effects are significantly enhanced due to the nonlinear coupling between the electrostatic and hydrodynamic force fields. This leads to the hydrodynamic scattering phenomena which can only be analysed numerically in the general case. As a result of hydrodynamic scattering the maximum coverage attained after long deposition time decrease considerably with increasing flow rate which can be described by Eq. (72). Accordingly, the higher coverage can only be attained for low *Re* number flows which was also demonstrated experimentally.

Although the mean features of the hydrodynamic blocking were confirmed there is still need for additional experiments to be performed for other flow configuration, especially for the simple shear.

Acknowledgements

References

[1] Z. Adamczyk, T. Dąbroś, J. Czarnecki, T.G.M. van de Ven, Adv. Colloid Interface Sci. 19 (1983) 183.

[2] Z. Adamczyk, Colloids Surf. 39 (1989) 1.

[3] Z. Adamczyk, B. Siwek, M. Zembala, P. Belouschek, Adv. Colloid Interface Sci. 48 (1994) 151.

[4] T. Dąbroś, T.G.M. van de Ven, Colloid Polym. Sci. 261 (1983) 694.

[5] T. Dąbroś, T.G.M. van de Ven, Physicochem. Hydrodyn. 8 (1981) 161.

[6] Z. Adamczyk, M. Zembala, B. Siwek, J. Czarnecki, J. Colloid Interface Sci. 10 (1986) 188.

[7] Z. Adamczyk, M. Zembala, B. Siwek, P. Warszyński, J. Colloid Interface Sci. 140 (1990) 123.

[8] Z. Adamczyk, L. Szyk, P. Warszyński, Colloids Surf. 75 (1993) 185.

[9] Z. Adamczyk, B. Siwek, L. Szyk, J. Colloid Interface Sci. 174 (1995) 130.

[10] Z. Adamczyk, L. Szyk, P. Warszyński, J. Colloid Interface Sci. 209 (1999) 350.

[11] U. Jonsson, I. Ronnberg, M. Malquist, Colloids Surf. 13 (1985) 333.

[12] J.C. Dijt, M.A. Cohen Stuart, J.E. Hofman, G.J. Fleer, Colloids Surf. 51 (1990) 141.

[13] H. Shirahama, J. Lyklema, W. Norde, J. Colloid Interface Sci. 139 (1990) 177.

[14] M.R. Bohmer, E.A. van der Zeeuw, G.J.M. Koper, J. Colloid Interface Sci. 197 (1998) 242.

[15] M.R. Bohmer, J. Colloid Interface Sci. 197 (1998) 251.

[16] J. Mellema, Curr. Opin. Colloid Interface Sci. 2 (4) (1997) 441 and Refs. within.

[17] T.G.M. van de Ven, Colloidal Hydrodynamics, Academic Press, London, 1989.

[18] M. Elimelech, J. Gregory, X. Jia, R. Williams, Particle Deposition and Aggregation, Butterworth–Heinemann, London, 1995.

[19] L.D. Landau, E.M. Lifszyc, Hydrodynamics, Polish ed., PWN, Warszawa 1994.

[20] M.E. Weber, D. Paddock, J. Colloid Interface Sci. 94 (1983) 328.

[21] H.C. Brinkman, Appl. Sci. Res. A. 1 (1947) 27.

[22] J. Happel, AIChE J. 4 (1958) 197.

[23] S. Kubawara, J. Phys. Soc. Jpn. 14 (1959) 527.

[24] A.C. Payatakes, R. Rajagopalan, C. Tien, J. Colloid Interface Sci. 49 (1974) 321.

[25] G. Neale, W.K. Nader, AIChE J. 20 (1974) 530.

[26] C.J. Guzy, E.J. Bonano, E.J. Davis, J. Colloid Interface Sci. 95 (1983) 523.

[27] Z. Adamczyk, T.G.M. van de Ven, J. Colloid Interface Sci. 84 (1981) 497.

[28] S. Varennes, T.G.M. van de Ven, Physicochem. Hydr. 9 (1987) 53.

[29] Z. Adamczyk, B. Siwek, M. Zembala, P. Warszyński, J. Colloid Interface Sci. 130 (1989) 578.

[30] M. Polverari, T.G.M. van de Ven, Langmuir 11 (1995) 1870.

[31] H. Takase, T.G.M. van de Ven, Colloids Surf. A 118 (1996) 115.

[32] P. Harwot, T.G.M. van de Ven, Colloids Surf. A 121 (1997) 229.

[33] A.D. Maude, Br. J. Appl. Phys. 12 (1961) 263.

[34] E. Bart, Chem. Eng. Sci. 23 (1968) 193.

[35] M.E. O'Neill, Mathematika 11 (1964) 67.

[36] M.E. O'Neill, Mathematika 14 (1967) 170.

[37] M.E. O'Neill, Chem. Eng. Sci. 23 (1968) 1293.

[38] W.R. Dean, M.E. O'Neill, Mathematika 10 (1963) 13.

[39] S.L. Goren, M.E. O'Neill, Chem. Eng. Sci. 26 (1971) 325.

[40] A.J. Goldman, R.G. Cox, H. Brenner, Chem. Eng. Sci. 22 (1967) 637.

[41] A.J. Goldman, R.G. Cox, H. Brenner, Chem. Eng. Sci. 22 (1967) 653.

[42] R. Cox, H. Brenner, Chem. Eng. Sci. 22 (1967) 1753.

[43] P. Warszyński, Adv. Colloid Interface Sci. 84 (1999) 47.

[44] Z. Adamczyk, M. Adamczyk, T.G.M. van de Ven, J. Colloid Interface Sci. 96 (1983) 135.

[45] K. Małysa, T.G.M. van de Ven, Int. J. Multiph. Flow. 12 (1986) 459.

[46] B.A. Alexander, D.C. Prieve, Langmuir 3 (1987) 778.

[47] T.G.M. van de Ven, P. Warszyński, X. Wu, T. Dąbroś, Langmuir 10 (1994) 3046.

[48] X. Wu, P. Warszyński, T.G.M. van de Ven, J. Colloid Interface Sci. 180 (1996) 61.

[49] X. Wu, T.G.M. van de Ven, Langmuir 12 (1996) 6291.

[50] J.R. Blake, Proc. Camb. Philos. Soc. 70 (1971) 303.

[51] T. Dąbroś, T.G.M. van de Ven, Int. J. Multiph. Flow. 18 (1992) 751.

[52] T. Dąbroś, Colloids Surf. 39 (1989) 127.

[53] T. Dąbroś, T.G.M. van de Ven, J. Colloid Interface Sci. 149 (1992) 493.

[54] K. Małysa, T. Dąbroś, T.G.M. van de Ven, J. Fluid. Mech. 162 (1986) 157.

[55] Z. Adamczyk, P. Weroński, Adv. Colloid Interface Sci. 83 (1999) 137.

[56] D.C. Prieve, E. Ruckenstein, AIChE J. 20 (1974) 117.

[57] Z. Adamczyk, T.G.M. van de Ven, J. Colloid Interface Sci. 97 (1984) 68.

[58] Z. Adamczyk, T. Dąbroś, J. Czarnecki, T.G.M. van de Ven, J. Colloid Interface Sci. 97 (1984) 91.

[59] Z. Adamczyk, J. Colloid Interface Sci. 78 (1980) 559.

[60] E. Ruckenstein, D.C. Prieve, J. Chem. Soc. Faraday II 69 (1973) 1522.

[61] L.A. Spielman, S.K. Friedlander, J. Colloid Interface Sci. 46 (1974) 22.

[62] B.D. Bowen, S. Levine, N. Epstein, J. Colloid Interface Sci. 54 (1976) 375.

[63] E. Ruckenstein, Colloid Interface Sci. 66 (1978) 531.

[64] Z. Adamczyk, B. Senger, J.C. Voegel, P. Schaaf, J. Chem. Phys. 110 (1999) 3118.

[65] B. Widom, J. Chem. Phys. 58 (1973) 4043.

[66] J. Feder, J. Theor. Biol. 87 (1980) 237.

[67] Y. Pomeau, J. Phys. A 13 (1980) 193.

[68] R.H. Swendsen, Phys. Rev. A 24 (1981) 504.

[69] E.L. Hinrichsen, J. Feder, T. Jossang, J. Stat. Phys. 11 (1986) 793.

[70] P. Schaaf, J. Talbot, J. Chem. Phys. 91 (1989) 4401.

[71] J. Talbot, G. Tarjus, P. Schaaf, Phys. Rev. A 40 (1989) 4808.

[72] J. Talbot, P. Schaaf, G. Tarjus, Molec. Phys. 72 (1991) 1397.

[73] J.W. Evans, Rev. Mod. Phys. 65 (1993) 1281.

[74] Z. Adamczyk, B. Siwek, M. Zembala, J. Colloid Interface Sci. 151 (1992) 351.

[75] Z. Adamczyk, P. Weroński, Langmuir 11 (1995) 4400.

[76] Z. Adamczyk, P. Weroński, J. Colloid Interface Sci. 189 (1997) 348.

[77] J.A. Barker, D. Henderson, J. Chem. Phys. 47 (1967) 4714.

[78] A.P. Thompson, E.D. Glandt, Phys. Rev. A 46 (1992) 4639.

[79] B. Senger, J.C. Voegel, P. Schaaf, A. Johner, A. Schmitt, J. Talbot, J. Chem. Phys. 97 (1992) 3813.

[80] A. Ansell, E. Dickinson, J. Chem. Phys. 85 (1986) 4079.

[81] B. Vincent, C.A. Young, Th.F. Tadros, J. Chem. Soc. Faraday I 76 (1980) 665.

[82] G.R. Joppien, J. Phys. Chem. 82 (1978) 2210.

[83] T. Arai, W. Norde, Colloids Surf. 51 (1990) 1.

[84] A.V. Engersma, R.L.J. Zsom, W. Norde, J. Lyklema, Colloids Surf. 54 (1991) 89.

[85] A.C. Juriaanse, J. Arends, J.J. Ten Bosch, J. Colloid Interface Sci. 76 (1980) 212.

[86] J.D. Aptel, J.C. Voegel, A. Schmitt, Colloids Surf. 29 (1988) 359.

[87] N. de Baillou, J.C. Voegel, A. Schmitt, Colloids Surf. 16 (1985) 271.

[88] J.D. Aptel, J.M. Thomann, J.C. Voegel, A. Schmitt, E.F. Bress, Colloids Surf. 32 (1988) 159.

[89] P. Wojciechowski, J.L. Brash, J. Biomat. Sci. Polymer Edn. 2 (1991) 203.

[90] F. Yan, Ph. Dejardin, Langmuir 7 (1991) 2230.

[91] M. Zembala, J.C. Voegel, P. Schaaf, Langmuir 14 (1998) 2167.

[92] H. Shirahama, J. Lyklema, W. Norde, J. Colloid Interface Sci. 139 (1990) 177.

[93] A.V. Elgersma, R.L.J. Zsom, J. Lyklema, W. Norde, Colloids Surf. 65 (1992) 17.

[94] W. Norde, E. Rouwendel, J. Colloid Interface Sci. 139 (1990) 169.

[95] M. Zembala, Ph. Dejardin, Colloids Surf. B 3 (1994) 119.

[96] J. Siollema, H.J. Busscher, Colloids Surf. 47 (1990) 323; Colloids Surf. 47 (1990) 337.

[97] J.M. Meinders, J. Noordmans, H.J. Busscher, J. Colloid Interface Sci. 152 (1992) 265.

[98] C.A. Johnson, A.M. Lenhoff, J. Colloid Interface Sci. 179 (1996) 587.

[99] M. Semmler, E.K. Mann, J. Rička, M. Borkovec, Langmuir 14 (1998) 5127.

[100] M. Elimelech, J. Colloid Interface Sci. 164 (1994) 190.

[101] P.R. Johnson, M. Elimelech, Langmuir 11 (1995) 801.

[102] J.J. Ramsden, Phys. Rev. Lett. 71 (1993) 295.